nature biomedical engineering

Article

https://doi.org/10.1038/s41551-024-01271-x

Spatially resolved subcellular protein–protein interactomics in drug-perturbed lung-cancer cultures and tissues

Received: 12 July 2023

Accepted: 25 September 2024

Published online: 30 October 2024

Check for updates

Shuangyi Cai[1,9], Thomas Hu[1,2,9], Abhijeet Venkataraman[1,3], Felix G. Rivera Moctezuma[4,5], Efe Ozturk[1,2,3], Nicholas Zhang[1,5], Mingshuang Wang[1,3], Tatenda Zvidzai[1], Sandip Das[1], Adithya Pillai[1], Frank Schneider[6,7], Suresh S. Ramalingam[7,8], You-Take Oh[7,8], Shi-Yong Sun[7,8] & Ahmet F. Coskun[1,5,7] ✉

Protein–protein interactions (PPIs) regulate signalling pathways and cell phenotypes, and the visualization of spatially resolved dynamics of PPIs would thus shed light on the activation and crosstalk of signalling networks. Here we report a method that leverages a sequential proximity ligation assay for the multiplexed profiling of PPIs with up to 47 proteins involved in multisignalling crosstalk pathways. We applied the method, followed by conventional immunofluorescence, to cell cultures and tissues of non-small-cell lung cancers with a mutated epidermal growth-factor receptor to determine the co-localization of PPIs in subcellular volumes and to reconstruct changes in the subcellular distributions of PPIs in response to perturbations by the tyrosine kinase inhibitor osimertinib. We also show that a graph convolutional network encoding spatially resolved PPIs can accurately predict the cell-treatment status of single cells. Multiplexed proximity ligation assays aided by graph-based deep learning can provide insights into the subcellular organization of PPIs towards the design of drugs for targeting the protein interactome.

Lung cancer is one of the leading causes of death, and non-small-cell lung cancer (NSCLC) accounts for 80% of lung cancer. One subgroup of patients with NSCLC harbouring epidermal growth-factor receptor (EGFR) mutation can benefit from EGFR tyrosine kinase inhibitors (TKIs), particularly osimertinib[1]. Despite there being advances in improving progression-free survival and overall survival, people can still develop acquired drug resistance due to the activation and crosstalk among signalling pathways. Hence, resolving the signalling dynamics and PPIs involved in EGFR-dependent cancer cell growth has become an important step to solving the problem of osimertinib resistance.

Phosphatidylinositol 3-kinase (PI3K)/protein kinase B (AKT)/mammalian target of rapamycin (mTOR) signalling is known as a key downstream pathway of EGFR, mediating resistance to EGFR TKIs[2]. The PI3K/AKT/mTOR pathway is commonly activated in NSCLC, and it also involves the development of chemoresistance in NSCLC by mediating with cluster of differentiation 147 (CD147)[3]. Another downstream pathway of EGFR, the mitogen-activated protein kinase (MEK)/extracellular

[1]Wallace H. Coulter Department of Biomedical Engineering, Georgia Institute of Technology and Emory University, Atlanta, GA, USA. [2]School of Electrical and Computer Engineering, Georgia Institute of Technology, Atlanta, GA, USA. [3]Parker H. Petit Institute for Bioengineering and Bioscience, Georgia Institute of Technology, Atlanta, GA, USA. [4]Woodruff School of Mechanical Engineering, Georgia Institute of Technology, Atlanta, GA, USA. [5]Interdisciplinary Bioengineering Graduate Program, Georgia Institute of Technology, Atlanta, GA, USA. [6]Department of Pathology and Laboratory Medicine, Emory University School of Medicine, Atlanta, GA, USA. [7]Winship Cancer Institute of Emory University, Atlanta, GA, USA. [8]Department of Hematology and Medical Oncology, Emory University School of Medicine, Atlanta, GA, USA. [9]These authors contributed equally: Shuangyi Cai, Thomas Hu. ✉e-mail: ahmet.coskun@bme.gatech.edu

signal-regulated kinase (ERK) signalling pathway, has been studied to delay or prevent acquired resistance to osimertinib. The crosstalk among these pathways is commonly measured by using western blot, flow cytometry, cell viability and apoptosis assays (Supplementary Fig. 1)[1]. The function of both pathways is widely described; however, the interaction between AKT/mTOR and ERK is still unclear. It has been demonstrated that reactivation of ERK1/2 occurs following EGFR TKI treatment, contributing to acquired resistance to osimertinib. The combination of EGFR TKI, osimertinib and MEK/ERK inhibitors could prevent the reactivation of ERK1/2 with a greater initial apoptotic response[1].

However, cancer relapse still develops due to the activation of yes-associated protein (YAP)/transcriptional coactivator with PDZ-binding motif (TAZ) activity, which are components of the Hippo pathway[4]. The Hippo pathway, a tumour-suppressive signalling pathway, could function as a resistant mechanism to EGFR and ERK/MEK inhibitors in EGFR mutant (EGFRm) NSCLC. In the absence of Hippo signalling, the inactivated large tumour suppressor kinase (Lats 1/2) results in the activation and translocation of YAP/TAZ into the nucleus, promoting the transcription of growth-related genes[5,6] (Supplementary Fig. 1). The interaction of YAP and transcriptional enhanced associate domain 1 (TEAD1) can be directly inhibited by verteporfin (VP)[7,8]. Thus, mechanisms of action on drug perturbations of PPI binding targets could serve as an alternative strategy to overcome multipathway resistance to osimertinib.

Inhibition in the ERK pathway may upregulate YAP/TAZ as a compensatory pathway. YAP can remain active upon inhibition of EGFR TKIs and EGFR/MEK inhibitors, and promote the cells to enter a senescence-like dormant state in the absence of EGFR downstream signalling in EGFRm NSCLC[4]. However, the crosstalk between the two pathways, especially the interaction between ERK and YAP/TAZ, is still unclear. Thus, unravelling the complexity of the PPIs or crosstalk among pathways at the subcellular level using a multiplex imaging approach is necessary to identify the signalling networks and spatial dynamics.

A protein-interaction network using affinity-purification mass spectrometry has been developed to map out physical associations among 90 tyrosine kinases[9]. Although this approach reveals previously unexplored EGFR network oncogenesis in lung cancer, the sample preparation with peptide extraction causes loss of spatial features in signalling. Also, PPIs have shown a capability in screening EGFR-dependent cancers using single-molecule pull-down and co-immunoprecipitation techniques. However, the single-molecule co-immunoprecipitation approach is limited to snap-frozen samples only[10]. Förster resonance energy transfer (FRET) has been used to detect PPIs on the basis of the energy transfer from a donor molecule to an acceptor molecule conjugated to antibodies. However, FRET requires the genetic modification of two proteins[11,12].

We overcome these limitations by directly targeting endogenous proteins using a proximity ligation assay (PLA). This method utilizes rolling cycle amplification (RCA) and permits the detection of PPIs. PLA is compatible with low-affinity antibodies to increase the sensitivity of biomarker detection with higher signal-to-noise ratios (SNRs)[13]. It also exhibits improved sensitivity and specificity for localizing proteins than western blot, sandwich enzyme-linked immunosorbent assay (ELISA)[14]. PLA has been used to investigate homodimerization and crosstalk between proteins[15–17]. Proximity sequencing (Prox-seq) has been developed, combining PLA with single-cell RNA sequencing, to quantify mRNAs, proteins and protein complexes[18]. However, high-throughput tools are needed to analyse the spatial context of PPIs. The signalling proteins display location-dependent functions in cells and tissues. In our study, we developed a multiplexed PLA assay, which we termed 'intelligent' sequential proximity ligation assay (iseqPLA), allowing us to detect multiple PPIs on the same sample and reveal the spatial PPI dynamics under different drug perturbations. iseqPLA visualizes the PPIs across AKT/mTOR, MEK/ERK and YAP/TEAD pathways in NSCLC EGFRm cell cultures and EGFRm frozen mouse tissue samples. Multiplexed spatial PPI dynamics studies under drug perturbations require computational frameworks for correlative and predictive modelling. Therefore, we demonstrated spatial PPI graph neural networks (spPPI-GNN) leveraging graph convolutional networks for single-cell-level prediction of drug perturbation from spatial PPI networks. Moreover, we performed correlative analysis approaches for quantifying PPI event co-localization and graph-based PPI networks with different protein markers.

Results

Multiplexed PPI detection using iseqPLA

To detect complex signalling interaction networks, we designed iseqPLA to provide highly sensitive maps of many PPIs in both cells and tissues (frozen or formalin-fixed paraffin-embedded (FFPE)). The detection can be either indirect or direct. For the detection of one PPI using direct labelling, the cells need to be stained with two primary antibodies targeting two different proteins or proteins phosphorylated at different sites[19,20]. These primary antibody pairs are conjugated to one of the PLA probes, one to PLUS and another to MINUS (Supplementary Fig. 2a). The PLA probe contains a unique oligonucleotide, is attached to the heavy chain of the primary antibody and permits the detection of PPIs in situ with a distance <20–40 nm at endogenous protein levels[21]. For indirect labelling where the oligonucleotides are conjugated to secondary antibodies, when the proteins of interest interact with each other, the DNA probes from two antibodies hybridize and ligate to form circular DNA[21]. Amplified circular DNA can be visualized using fluorescence microscopy. The commercial PLA detection kit allows us to visualize and quantify the individual PPI. We advanced the current PLA technique to overcome the limitation on the number of protein pairs that can be detected by the conventional microscope. iseqPLA can detect multiple PPIs by utilizing iterative cycles of labelling, imaging, treating with DNase I/Nuclease P1 and relabelling (Fig. 1a and Supplementary Fig. 2b). The oligonucleotides on primary antibodies are removed using DNase I/Nuclease P1. iseqPLA utilizes commercial DuoLink PLA or Navinci assays to detect highly multiplexed subcellular protein interaction maps. This iterative process can be repeated to create multiplexed signalling interaction maps in the same single cell. There are several ways to multiplex the PPI detection process. We could detect one pair of PPIs per cycle (Supplementary Fig. 3) or detect three pairs of PPIs per cycle using multicolour detection (Supplementary Fig. 4). Also, by utilizing a multispectral microscope, we could achieve the detection of more than 3 pairs of PPIs per cycle (Supplementary Fig. 5).

iseqPLA profiles multiple PPIs and their subcellular distributions in single cells. By incorporating the localization information of organelles and proliferation proteins using rapid multiplexed immunofluorescence (RapMIF) (Fig. 1a)[22], iseqPLA visualizes the protein associates across AKT/mTOR, MEK/ERK and YAP/TEAD pathways at subcellular levels in NSCLC EGFRm cell cultures and frozen mouse tissue samples. iseqPLA experiments of cell cultures treated with osimertinib demonstrate the PPI dynamics and responses involved in the signalling pathways. The spPPI-GNN framework successfully predicts the cell perturbation states from the underlying PPI network graph created using PPI event distances. To validate our model, we compared our spPPI-GNN model with traditional machine learning (ML) models using PPI event counts, a multilayer perception (MLP) model using PPI counts and a multi-instance learning (MIL) model using multilayer perception (Fig. 1b).

We evaluated the sensitivity, specificity and batch consistency of iseqPLA, as well as the effect of osimertinib on protein baseline or PPI level (Extended Data Fig. 1a). To investigate the sensitivity of PLA, the kinetic change in PPI expression was measured in response to a range of 12-h osimertinib treatments in HCC827 EGFRm NSCLC cells (Supplementary Fig. 6a,b). Cyclin D1/cyclin-dependent kinases 4 (Cdk4)

https://doi.org/10.1038/s41551-024-01271-x

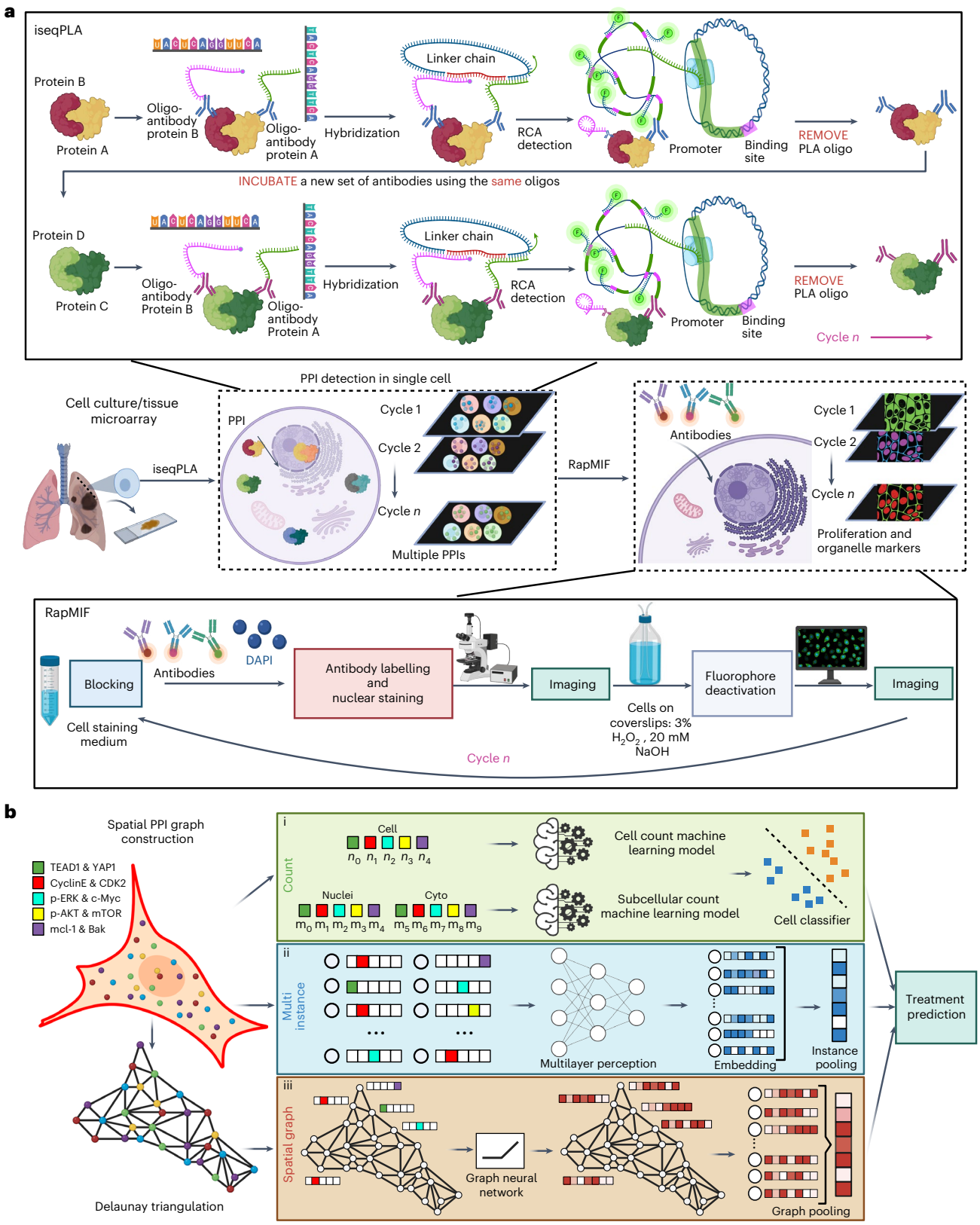

Fig. 1 | Schematic illustration of iseqPLA for subcellular spatial-signalling networks. a, Schematic of iseqPLA combined with RapMIF in cell cultures or tissues. PPIs in either cell cultures or tissue samples are detected using iseqPLA. Each PPI is detected by primary antibodies conjugated with oligonucleotides. Between cycles, the probes are removed using the enzyme. Following *n* cycles, multiple PPIs are measured at the subcellular level in single cells. RapMIF is then utilized to visualize proliferation, signalling and organelle markers. **b**, Spatial PPI graph construction. **(i)** Counting using machine learning models, where each cell PPI count is used as model input to predict without spatial information. **(ii)** Multi-instance learning at the cell level with a multilayer perception network, where PPIs are treated as a bag of instances without spatial information. **(iii)** The proposed spPPI-GNN network that utilizes single-cell spatial PPI graph for prediction, where the PPI spatial graphs are used as input for the model prediction. Created with BioRender.com.

PPI decreased as the osimertinib concentration was increased from 0 to 100 nM, indicating that osimertinib inhibits cell cycle progression and proliferation (Extended Data Fig. 1b and Supplementary Fig. 6c). However, the decreasing trend was moderate for SRY-Box transcription factor 2 (Sox2)/Octamer-binding transcription factor 4 (Oct4), phosphor-p90 Ribosomal S6 Kinase (p-p90RKS)/Nuclear factor kappa B (NF-kB) and BCL2-interacting mediator of cell death (Bim)/translocase of outer membrane (Tom20) due to the lower copy numbers of PPIs, which are sensitive to PPI binding fluctuations.

To measure and quantify the specificity of the multicolour PLA, we performed Bim/Tom20 PPI on HCC827AR/BimKO cells, which are osimertinib-resistant cells with Bim knockout, and HCC827AR empty vector as a control (Supplementary Fig. 7a and Dataset 1). The Bim intensity was also measured using immunofluorescence (IF) (Supplementary Fig. 7b). A reduction in Bim/Tom20 PPI counts was observed in the cytosol of HCC827AR/BimKO cells (Extended Data Fig. 1c and Supplementary Fig. 7c). The few positive signals of Bim/Tom20 in HCC827AR/BimKO cells may come from the stochastic binding of the Bim primary antibody in the nucleus. Nucleus IF staining of Bim in HCC827AR/BimKO cells also confirmed the IF noisy staining of the Bim antibody (Supplementary Fig. 7b,c). Overall, the downregulation of Bim/Tom20 PPIs and Bim mean intensity in HCC827AR/BimKO cells indicates the specificity of PLA (Extended Data Fig. 1c and Supplementary Fig. 7c). To evaluate the specificity of single-colour PLA (Supplementary Dataset 2), HCC827 cells were also stained with the anti-p-ERK-PLUS probe, then anti-YAP MINUS probe, followed by a positive control, Cyclin E/cyclin-dependent kinases 2 (Cdk2) (Supplementary Fig. 7d). Negative results from the staining of only PLUS or MINUS probes validated the specificity of PLA (Supplementary Fig. 7e).

To investigate whether osimertinib inhibits the baseline protein expression or the PPI, we performed IF to visualize and quantify the baseline protein levels and utilized PLA to measure the corresponding PPI counts in untreated and osimertinib-treated HCC827 cells (Extended Data Fig. 1a and Supplementary Fig. 8). Osimertinib effectively inhibited the expression of Sox2/Oct4 interactions; however, there was no effect on the baseline protein expression level (Extended Data Fig. 1d). This indicates that osimertinib may affect the PPI without changing the baseline expression of proteins. However, osimertinib inhibits cyclin D1 but upregulates CDK4, resulting in the unchanged interaction between the two proteins (Extended Data Fig. 1d). Cyclin D1 expression levels fluctuate across the cell cycle, while CDK4 remains relatively consistent. The interaction between cyclin D1 and CDK4 plays a key role in the S-phase cell cycle progression[23]. The cyclin D1/CDK4 pair could be a potential target for combinatorial treatment of osimertinib. Osimertinib as a TKI can directly inhibit EGFR phosphorylation, thereby altering the dynamics of the downstream signal cascades, AKT/mTOR, ERK/MEK and Hippo pathways. Whether the baseline protein levels or the interactions involved in the signal cascades are perturbed in response to osimertinib treatment needs further study and statistical support.

To examine the batch consistency of iseqPLA, we performed two cycles of iseqPLA using multicolour detection in a total of 4 pairs of protein interactions (Cycle 1: Sox2/Oct4 and NF-kB/p-P90rsk; Cycle 2: cyclin D1/CDK4 and Bim/Tom20) on HCC827 cells across two batches (Supplementary Fig. 9a,b). Between cycles, the signals were removed using nuclease P1 (Supplementary Fig. 9a,b). Cells at passages 10 and 21 from different batches demonstrated a similar trend across four PPIs (Extended Data Fig. 1e and Supplementary Fig. 9c), indicating the batch consistency of iseqPLA.

Highly multiplexed spatial PPI networks in EGFRm cells

To reconstruct the signalling networks and PPI in EGFRm cells under drug perturbations, iseqPLA was used to profile 5 PPIs involved in the AKT/mTOR, MEK/ERK and YAP/TEAD pathways in the NSCLC EGFRm osimertinib-sensitive cell line, HCC827 cells. DNase I was used to remove probes between cycles. In our study, we first investigated whether the EGFR pathways would be affected by osimertinib in HCC827 cells, eventually affecting cell proliferation and growth. HCC827 cells were treated with and without 100 nM osimertinib for 6, 12 and 24 h (Supplementary Fig. 10a). The clinically achievable steady-state plasma concentration of osimertinib is ~500 nM in patients with EGFRm NSCLC receiving an 80 mg day^{-1} dosage[24]. The concentration of 100 nM osimertinib should fall within the expected range of steady-state plasma levels of osimertinib and has been selected to ensure sufficient inhibition of the target pathway to mimic clinically relevant dosing levels. p-ERK was used to indicate the efficacy of osimertinib treatment. P-ERK was suppressed initially after a 6-h treatment; however, osimertinib even increased p-ERK after a 12-h treatment (Supplementary Fig. 10b and Dataset 3), suggesting that osimertinib may exert transient inhibitory effects on the MEK/ERK pathway. To reveal the PPI dynamics under osimertinib treatment, we performed iseqPLA on HCC827 cells treated with and without 100 nM osimertinib for 12 h. To determine the best staining conditions for both RapMIF and iseqPLA, we performed titrations on each antibody in the multiplexed panel. IF was performed to evaluate antibody staining using two different dilution rates (Supplementary Figs. 11 and 12). We compared the SNRs of these IF images and used the conditions with higher SNRs for either iseqPLA or RapMIF experiments (Supplementary Table 1). The staining dilutions were consistent with the manufacturer-suggested dilution range.

By using iseqPLA, we showed and compared PPI dynamics among proteins including YAP/TEAD1, cyclin E/CDK2, p-ERK/cellular myelocytomatosis (c-Myc), myeloid cell leukaemia sequence 1 (Mcl-1)/Bcl-2 antagonist killer 1 (Bak) and p-AKT/mTOR (Supplementary Fig. 13). The PPI distributions were visualized using their spatial localization. Each node represents one detected PPI event, and for each single cell, a spatial graph of PPI events was constructed using Delaunay triangulation (see Methods) which captures the underlying spatial neighbouring information of PPI events. The cell boundary was obtained from segmentation on the p-EGFR signalling protein (Fig. 2a).

We first examined the effect of osimertinib on cell apoptosis and proliferation by comparing the cyclin E/CDK2 and Mcl-1/Bak interactions. MCL-1 is known as an anti-apoptotic factor, and it can be phosphorylated by ERK, resulting in enhanced proteasome-dependent degradation. Osimertinib downregulates Mcl-1, thereby enhancing cell apoptosis[25]. Mcl-1 can sequester Bak activity via direct interaction, thereby preventing cell apoptosis[26]. The interaction between Mcl-1 and Bak is related to the inhibition of cell apoptosis. After osimertinib treatment, the cells did not exhibit a significant change in the Mcl-1/Bak interaction in either the cytoplasm or the whole cell (Fig. 2b, Supplementary Figs. 14 and 15a and Dataset 4). However, osimertinib effectively inhibited the interaction between cyclin E and CDK2 (Fig. 2b and Supplementary Fig. 15a), which functions in initiating the S phase and cell proliferation[27].

We next determined the effects of osimertinib on EGFR-related signalling pathways. Osimertinib as an inhibitor to EGFR downregulated the p-AKT/mTOR pathway reducing the interactions in the cytoplasm (Supplementary Fig. 15a). Osimertinib can induce the degradation of c-Myc, which regulates cell growth and proliferation in EGFRm-sensitive cells, and ERK can phosphorylate c-Myc at S62 linked to c-Myc's stabilization[28]. However, the inhibitory effect is limited in osimertinib-resistant cell lines, and the upregulation of c-Myc is related to acquired resistance to osimertinib[28]. In terms of the YAP/TEAD1 pathway, YAP can remain active under EGFR TKIs and EGFR/MEK inhibitions contributing to tumour dormancy in EGFRm NSCLC[4]. We observed that after treatment, the cells exhibited significantly increased the interactions of YAP/TEAD1 and P-ERK/c-Myc (Fig. 2b), indicating that osimertinib may change the signalling dynamics by upregulating the YAP and ERK pathways to compensate for EGFR inhibition. Previous studies examining the effect of osimertinib on p-ERK using western blot demonstrated the inhibitory role of osimertinib on p-ERK for up

https://doi.org/10.1038/s41551-024-01271-x

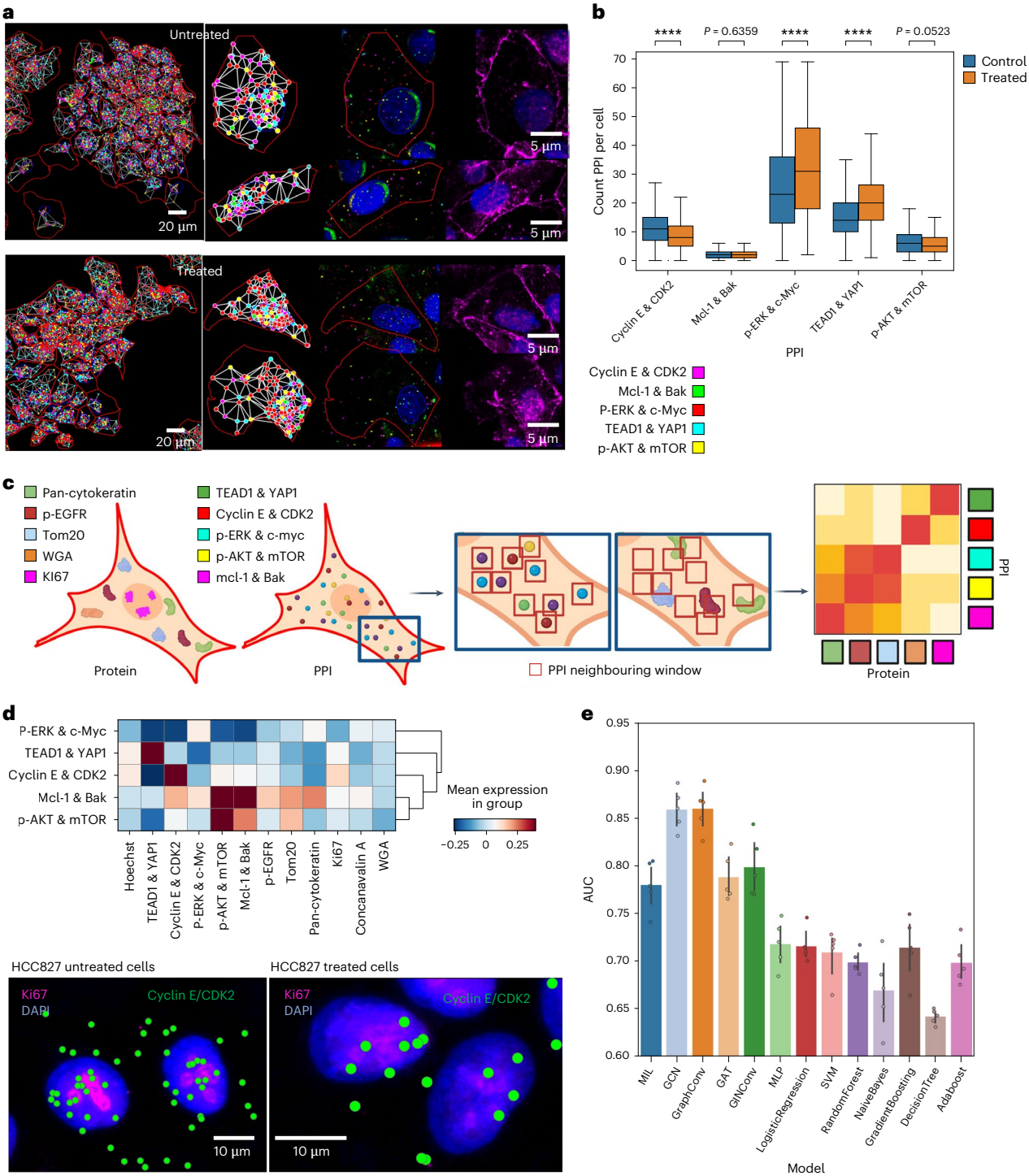

Fig. 2 | PPI networks, co-expression analysis and predictive models of 16-plex profiling for 5 PPIs and 6 signalling and organelle markers in HCC827 cells. **a**, Columns from left: Col. 1: the large field-of-view (FOV) demonstrates the network analysis of 5 PPIs across 5 cycles in HCC827 cells without treatment and with 100 nM osimertinib treatment for 12 h. The total cell number is 951 for untreated and 560 for treated cells. Col. 2: examples of networks in individual cells. Each node presents a PPI event and Delaunay triangulation was performed to connect nodes. Col. 3: distribution of 5 PPIs in raw images; the red outline is the p-EGFR. Col. 4: the cell boundary in magenta is p-EGFR IF staining. **b**, Quantification of PPI counts in HCC827 cells treated with and without osimertinib. The separate PPI counts comparison in cytosol and nuclei is shown in Supplementary Fig. 15a. Statistical testing was performed using two-sided Mann–Whitney Wilcoxon test (****$P \leq 0.0001$). **c**, Data analysis workflow. The expression and spatial distribution of protein markers, as well as the localization of PPIs, were detected using iseqPLA and RapMIF. The mean expression of these proteins in each PPI neighbouring window with a size of 5 in radius was calculated. Created with BioRender.com. **d**, Normalized co-expression of 5 PPIs with the mean intensity of 6 protein markers in single cells. The normalized co-expression in cytosol and nuclei is shown in Supplementary Fig. 15b. The images at the bottom show two examples of the co-expression of ki67 and cyclin E/cdk2 PPI represented in scatter dots from untreated and osimertinib-treated HCC827 cells. **e**, Comparison of AUC scores between the spPPI-GNN, ML, MIL and MLP models for prediction of single-cell treatment status in the 5-PPI dataset. GCN and GraphConv layer-based spPPI-GNN show the best overall scores. Box plots in **b**: median (horizontal line inside box), 25th and 75th percentiles (box), 25th and 75th percentiles ±1.5 times the interquartile range (whiskers). Bar graphs in **e**: mean ± 95% CI.

to 24 h using western blot[1]. However, western blot measures the total protein level, which is different from the protein interactions where proteins function in active forms.

To resolve the spatial proteomics and PPIs, we also integrated RapMIF into our panel[22]. RapMIF was utilized to detect the localization of distinct organelles (such as Golgi: wheat germ agglutinin (WGA), endoplasmic reticulum: Concanavalin A, mitochondria: TOM20, nucleus: DAPI). The organelle information can be associated with the distribution of PPIs from iseqPLA to identify the subcellular localization of PPIs (receptors, cytosol or nucleus) in individual cells (Fig. 2c). The PPI co-expression confirmed the localization of Mcl-1/Bak interactions in mitochondria with high co-expression of TOM20 (Fig. 2d). We also observed the co-expression of cyclin E/CDK2 and ki67 in the nucleus (Fig. 2d, Supplementary Fig. 15b and Dataset 5). All three markers are related to cellular proliferation and they are highly correlated with each other in colorectal carcinoma[29]. Also, iseqPLA revealed the co-localization of Mcl-1/Bak and p-AKT/mTOR PPIs (Fig. 2d). This is potentially due to the regulation of the AKT pathway in mitochondria-mediated functions such as redox states, apoptosis and metabolism[30].

We investigated the distribution of PPI events as predictive features to respond to drug treatment by training graph-based models to predict the treatment output on the basis of the PPI-event counts. We developed SpPPI-GNN, a predictive pipeline built on experimentally identified PPI events of interest, facilitated by iseqPLA and RapMIF. The primary objective is to predict cellular treatment states and extract distinctive PPI spatial subcellular graphs indicative of treatment states, enhancing our understanding of the impact of drugs on cellular pathways.

Current graph neural network (GNN) models focus on predicting protein interactions from amino-acid sequences. Models such as GraphPPIS[31] and SGPPI[32] are designed to predict PPI probabilities. In summary, spPPI-GNN is tailored to address inquiries at the cellular level, whereas GraphPPIS and SGPPI are designed for inquiries at the protein level (Supplementary Fig. 16). Other GNN models are designed for cellular-level tasks, such as PLA_GNN[33] for predicting subcellular protein mislocation using a graph of proteins, spaGNN[34] for predicting cell identity with RNA graphs, as well as newly developed GNN for pathway analysis tasks[35].

SpPPI-GNN encodes intracellular PPIs as nodes and utilizes Delaunay triangulation for spatial location to form edges (Methods and Extended Data Fig. 2a). The subcellular spatial graph is used in the graph neural network forward step by combining the graph neural network level and the neighbouring node embedding. Finally, all PPI event node information is combined using a graph pooling layer for predicting cell-level treatment information. The raw count of PPI events provides a comprehensive characterization of cellular state, and subcellular PPI spatial graphs contain important information on the underlying PPI spatial distribution (Extended Data Fig. 2b,c). Moreover, we compared various GNN layers, hidden layer sizes, number of layers and graph pooling layers to comprehensively compare the different models (Methods, Supplementary Fig. 17a and Datasets 6 and 7). The sensitivity of each parameter was examined by holding all other hyperparameters constant and varying only one hyperparameter at a time (Supplementary Fig. 18a and Table 2). The sensitivity analysis focused on various hyperparameters, including graph pooling methods, hidden layer sizes, the number of layers, graph types and the comparison between two-dimensional (2D) and 3D graphs, providing a comprehensive view of the model's robustness and adaptability to parameter changes. The resulting area under the curve (AUC) scores were calculated by taking the mean of the scores across different parameter settings, ensuring a comprehensive evaluation of each model's performance. The analysis demonstrated a large variation in model AUC scores when adjusting the pooling layer hyperparameter.

We benchmarked the spPPI-GNN model prediction AUC score with machine learning (ML) models on mean PPI event counts per cell, multilayer perception (MLP) models on mean PPI event counts per cell and a multi-instance-learning (MIL) MLP model on subcellular PPI event information without spatial graph (Methods). The AUC scores show that spPPI-GNN models outperform ML, MLP and MIL models in predicting cell treatment states from subcellular information (Fig. 2e).

Scaling up the profiling of signalling networks

To confirm the feasibility of scaling up the PPI detection, we profiled 9 PPIs in HCC827 cells treated with and without osimertinib for 12 h. The cells were profiled with 2 cycles of multicolour detection, followed by 5 cycles of single colour detection of PPIs (YAP/TEAD1, cyclin E/CDK2, p-ERK/c-Myc, p-AKT/mTOR, Mcl-1/Bak). The multicolour detection allows us to detect 2 to 3 pairs of PPIs in a single cycle. RapMIF was performed to detect organelle locations, cell proliferation and tumour cells, followed by iseqPLA. The PPI distribution in every single cell can be visualized using the spatial network (Supplementary Figs. 19 and 20).

We observed that the later cycles of iseqPLA in the 9-PPI dataset, such as TEAD1/YAP and cyclin E/CDK4, exhibited much fewer signals. This is important because DNase I digests DNA that is connected to proteins in the nucleus, especially transcription factors. To minimize the DNase I effect on nuclear proteins, we changed the order of PPI detections and observed that TEAD1/YAP and cyclin E/CDK4 PPIs were not affected in the first two cycles (Supplementary Fig. 13). We observed that multicolour PPI detection was less sensitive to DNase I and bleaching, and we were able to redetect the residuals of PPIs after 6× treatment with DNase I and bleaching (Supplementary Fig. 21).

To preserve the quality of single-colour PPI detection, nuclease P1 as an alternative reagent to DNase I to digest single-strand DNA was tested on 5 pairs of PPIs using single-colour detection in HCC827 untreated cells (Supplementary Fig. 22). Nuclease P1 concentrations ranging from 1:500 to 1:100 worked effectively in removing single-stranded DNAs bound to fluorophores. In addition to nuclease P1, we also demonstrated that shortening the DNase I incubation from 4 to 2 h can still remove the oligos and fluorophores. Dimethylsulfoxide (DMSO) stripping solution exhibited practicability in deactivating the signals[36]. By restaining the samples with another set of PPIs, we confirmed the feasibility of multiplexing PPIs using nuclease P1 and DMSO stripping approaches. We also observed that nuclease P1 has a lower effect on phalloidin by preserving its phenotype compared with DNase I and DMSO.

Therefore, we further scaled up iseqPLA using nuclease P1 to detect 13 PPIs in HCC827 cells treated with and without osimertinib for 12 h. The cells were profiled with 4 cycles of multicolour and then 5 cycles of single-colour detection, followed by multiplexed immunofluorescence (Fig. 3a,b and Supplementary Fig. 23). Compared with DNase I, nuclease P1 better preserves the nuclear structure (Supplementary Fig. 24). However, we observed some blobs (larger than a typical PPI dot size) in the nucleus, which were digitally identified and corrected in PPI reconstructions.

In addition to cyclin E/CDK2, cyclin D1/CDK4 was used to detect the G1/S transition in the cell cycle[37]. Osimertinib exhibited an inhibitory effect on cyclin D1/CDK4 (Fig. 3c). Orthogonal assays confirmed the multiplexed PPI signals and the efficacy of the osimertinib treatment. Similar upregulation patterns of p-ERK/c-Myc after treatment in 13-PPI data were demonstrated (Fig. 3c) compared with 5-PPI data. Osimertinib inhibited p-ERK and c-Myc baseline-level expression (Extended Data Fig. 3a,b). The downregulation of p-ERK after osimertinib treatment in HCC827 cells was further demonstrated by Luminex data (Extended Data Fig. 3c,d) of the cell lysates. The upregulation of p-ERK shown in the IF results may be due to the heterogeneity of expression of p-ERK in the subpopulation of HCC827 cells (Supplementary Fig. 10b). P-ERK/c-Myc interactions displayed heterogeneous distribution in the HCC827 cells (Extended Data Fig. 3e and Supplementary Fig. 25). P-ERK/c-Myc PPI events were quantified across several regions of interest (ROIs), and the coefficient of quartile variation demonstrated the dispersion of PPI event distribution in each ROI (Supplementary

Fig. 25b,c and Dataset 8). To validate the p-ERK/c-Myc interaction, we performed co-immunoprecipitation (co-IP) on p-ERK and c-Myc in HCC827 cells, demonstrating the upregulation of p-ERK/c-Myc interactions after osimertinib treatment (Extended Data Fig. 3b). We also examined the interaction between p-p90RSK and NF-κB p65. P-p90RSK as an ERK substrate phosphorylates p65 at S276 in an ERK-dependent manner, leading to inflammation response[38]. Osimertinib effectively inhibited the PPIs of NF-κB/p-p90RSK. Sox2 as a transcription factor can be incorporated with Oct4 to maintain stem-like properties. The downregulation of sox2/oct4 demonstrates the inhibitory effect of osimertinib in EGFRm-sensitive cells (Fig. 3c, Supplementary Figs. 26–28a and Dataset 9). However, it has been found that osimertinib-resistant EGFRm NSCLC cell lines express high levels of sox2 and increased autophagy[39,40]. To evaluate cell apoptosis, in addition to Mcl-1/Bak, we also profiled the interaction between Tom20 and Bim. Bim as a pro-apoptotic Bcl-2-family protein can interact with Tom20 independent of the binding to anti-apoptotic proteins[41]. Tom20 protein is inserted in the outer mitochondria membrane (OMM) and may function in the regulation of Bim localization into mitochondria. Reduced interactions between Tom20 and Bim were observed after 12 h of osimertinib treatment (Fig. 3c). However, Bim may translocate into OMM without TOM receptors and Tom20 also mediates the transfer of anti-apoptotic Bcl-2 proteins into mitochondria[41,42]. More studies are needed to conclude whether osimertinib enhances cell apoptosis in HCC827 cells. Osimertinib inhibited the interaction of EGFR/Grb2 (Fig. 3c). The interaction between EGFR and Growth-factor receptor-bound protein 2 (Grb2) is required for EGFR mutant cells survival, and it is related to sensitivity to EGFR inhibition[43]. The binding of Tumour necrosis factor-related apoptosis-inducing ligand (TRAIL) to Death receptor 5 (DR5) can trigger cell apoptosis[44]. However, there was no significant difference in TRAIL/DR5 and AKT/Forkhead box protein O1 (FOXO1) PPI counts after osimertinib treatment (Fig. 3c and Supplementary Fig. 28a). FoxOs regulate cell cycle arrest and apoptosis. The direct phosphorylation of FoxOs by AKT can result in FoxOs inactivation and accumulation in the cytoplasm[45]. The non-significance of AKT/FoxO1 interaction may indicate the minimal effect of EGFR TKI on p-AKT and FoxO1 interaction (Fig. 3c)[46]. AKT inhibitors could effectively inhibit AKT and FoxO1 (ref. 46). We observed low PPI events from SIRT1/p53 (Fig. 3c and Supplementary Fig. 28a). Tumour protein p53 (P53) is a tumour suppressor that promotes apoptosis. Sirtuin 1 (SIRT1) might act as a tumour promoter by directly inhibiting p53 through the deacetylation of p53. Hypoxia can upregulate the expression of SIRT1, and the long-term hypoxia may contribute to the resistance to osimertinib in NSCLC cells[47]. The low PPI events may be due to the opposite staining patterns of SIRT1 and p53, cytosolic IF signals of SIRT1 and nuclear staining of p53, resulting in the negative results of SIRT1/P53 PPI. These results further confirmed the specificity of PLA.

Cyclin E/CDK2 co-localizes in the Golgi with high co-expression of NBD-C6 (Fig. 3d, Supplementary Fig. 28b and Datasets 7 and 10). Cyclin E regulates the transition from the G1 to the S phase in the cell cycle. The activity of cyclin E can be directly regulated by RhoBTB3, a Golgi-localized and -associated protein. The direct interaction between cyclin E and RhoBTB3 mediates the ubiquitylation and turnover of cyclin E during the S phase[48]. Also, the co-expression between p-AKT/mTOR and NBD-C6 in cytosol demonstrates the potential regulation of mTOR signalling by Golgi (Fig. 3d). Golgi can modulate mTOR activity in several ways, including downregulating autophagy by activating mTOR, and Golph2, a Golgi protein, has been found to promote mTOR activity through the PI3K/AKT pathway[49].

Similarly, we compared ML, MLP and ML with spPPI-GNN models for the prediction of drug treatment from both the subcellular information and PPI quantification (Supplementary Fig. 17b and Dataset 11). Using the same parameter search method as previously described, integrating the spatial graphs with PPI quantification achieved a better model performance, with a higher AUC score in spPPI-GNN models (Methods and Fig. 3e). We also conducted sensitivity analysis of the parameters used in different models in the 13-PPI data (Supplementary Fig. 18b and Table 2). The variation in the model AUC scores when adjusting the pooling layer hyperparameter is smaller with 13 PPIs than with 5 PPIs.

We performed a similar data analysis on 9-PPI datasets and obtained similar results (Supplementary Figs. 29 and 30). However, we obtained distinct downregulation patterns for p-ERK/c-Myc after treatment in 9-PPI data (Extended Data Fig. 4a) compared with 5-PPI data. This is probably due to the subpopulation heterogeneity among cells, and p-ERK/c-Myc exhibited a relatively higher expression level in the 5-PPI dataset from the uniform manifold approximation and projection (UMAP; highlighted in red in Extended Data Fig. 4b). From the image, we observed the Cytochrome C oxidase subunit 4I1 (Cox IV), a mitochondria marker that co-localizes with Bim/Tom20 PPI (Supplementary Fig. 31a), confirming the location of Bim/Tom20 interaction in mitochondria. Due to the non-uniform signals of Cox IV in the large ROI, we filtered out the Cox IV positive regions for co-expression and correlation analysis. No co-localization was observed between Bim/Tom20 and Cox IV (Supplementary Fig. 31b,c and Datasets 12 and 13). This is potentially due to the large-scale normalization overlooking the co-expression variety. We performed the co-expression analysis between 5 relatively highly expressed PPIs and 8 protein markers and confirmed the co-localization between Bim/Tom20 and Cox IV (Supplementary Fig. 31d and Dataset 14).

Similarly, we compared ML, MLP and ML with spPPI-GNN models for the prediction of cell drug perturbation from subcellular information (Supplementary Fig. 17c and Datasets 15 and 7). Using the same parameter search method as previously described, we obtained the prediction AUC score using PPI events spatial graphs (Methods). The overall prediction results showed higher AUC using spPPI-GNN compared with other benchmark models (Supplementary Fig. 31e and Dataset 16). The sensitivity of various parameters regarding model prediction variability was also calculated (Supplementary Fig. 18c and Table 2). Overall, the pooling layer hyperparameter displayed a higher sensitivity compared with other hyperparameters.

We also visualized the small groups of interconnections among PPIs using network motifs in the 5 and 9-PPI datasets. These network motifs are statistically significant patterns within large spatial-signalling

Fig. 3 | Quantification, co-expression and modelling of 34-plex profiling for 13 PPIs and 8 signalling and organelle markers in HCC827. a, Schematic illustration of 34-plex iseqPLA. HCC827 cells with and without 12-h 100-nM osimertinib treatment were stained with 4 cycles of multicolour PLA and 5 cycles of single-colour PLA, followed by cell phenotyping. The total cell number is 1,029 for untreated and 978 for treated cells. Created with BioRender.com. **b**, Top left: visualization of 5 PPIs overlaid with p-EGFR and DAPI. Bottom: network analysis of 13 PPIs across 9 cycles in HCC827 cells without treatment and with 100 nM osimertinib for 12 h. Each node presents a PPI event, and Delaunay triangulation was performed to connect nodes. The cell boundary in red is p-EGFR IF staining. The overlay of signalling, proliferation and organelle markers is illustrated. **c**, Comparison of PPI counts in osimertinib-treated and untreated HCC827 cells. The separate PPI counts comparison in cytosol and nuclei is shown in Supplementary Fig. 28a. Statistical testing was performed using two-sided Mann–Whitney Wilcoxon test (****$P \leq 0.0001$). **d**, Top: normalized co-expression of 13 PPIs with the mean intensity of 7 protein markers in single cells. The normalized co-expression in cytosol and nuclei is shown in Supplementary Fig. 28b. Bottom: two examples of co-expression of PPIs represented in scatter dots, and Cox IV in untreated and treated HCC827 cells. **e**, Comparison of AUC scores between the spPPI-GNN, ML, MIL and MLP models for prediction of single-cell treatment status in the 13-PPI dataset. GCN and GraphConv layer-based spPPI-GNN show the best overall scores. Box plots in **c**: median (horizontal line inside box), 25th and 75th percentiles (box), 25th and 75th percentiles ±1.5 times the interquartile range (whiskers). Bar graphs in **e**: mean ± 95% CI.

https://doi.org/10.1038/s41551-024-01271-x

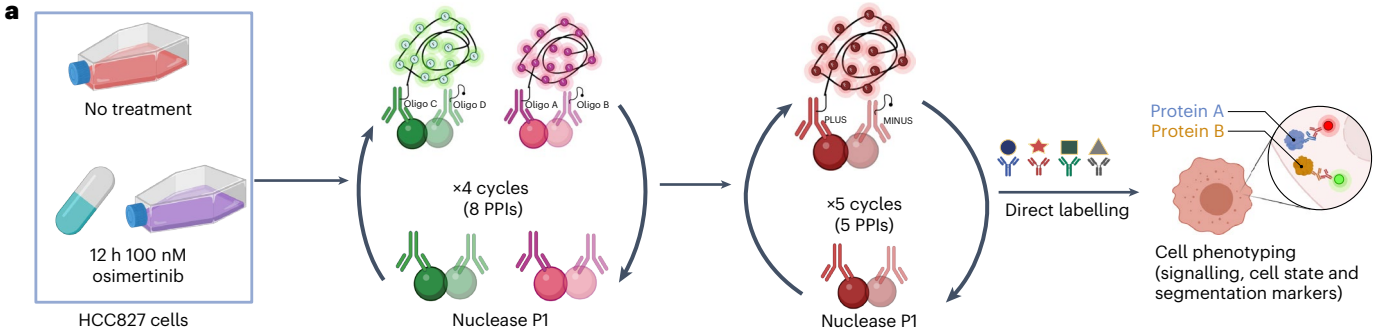

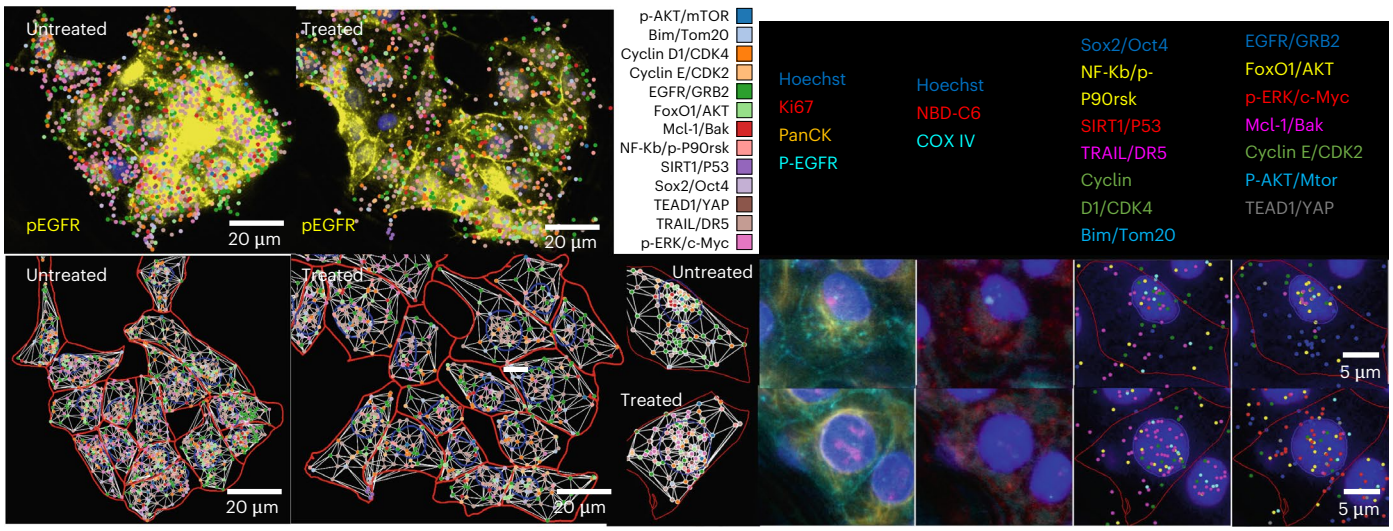

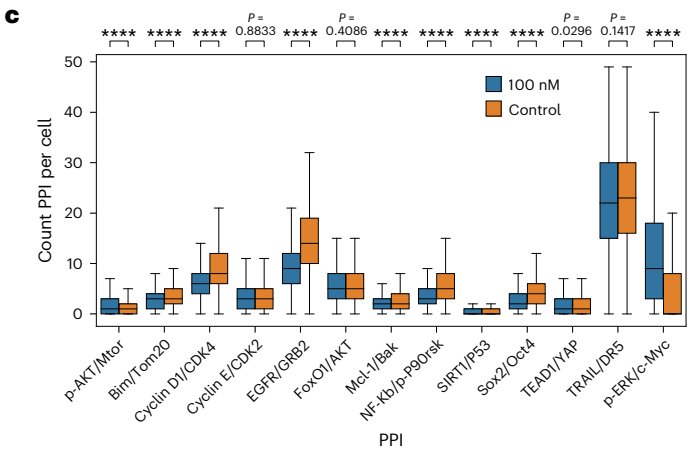

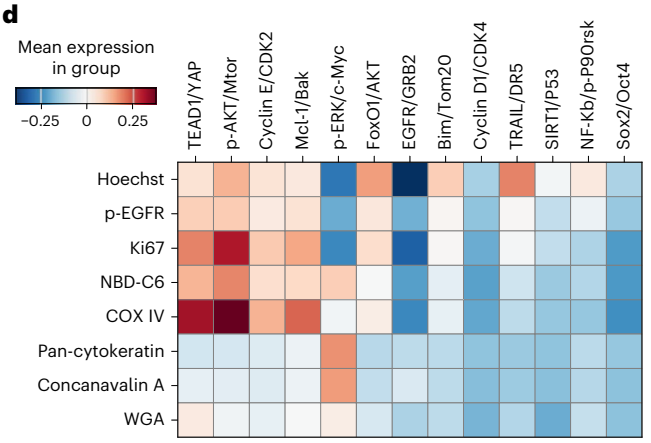

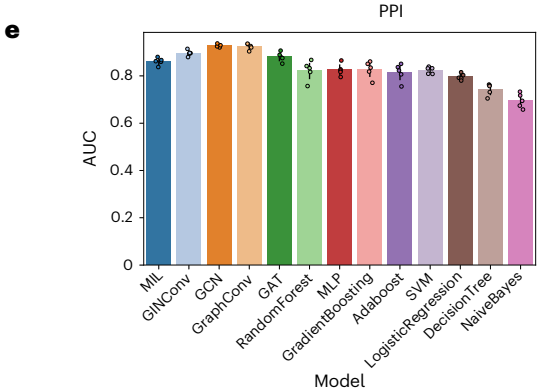

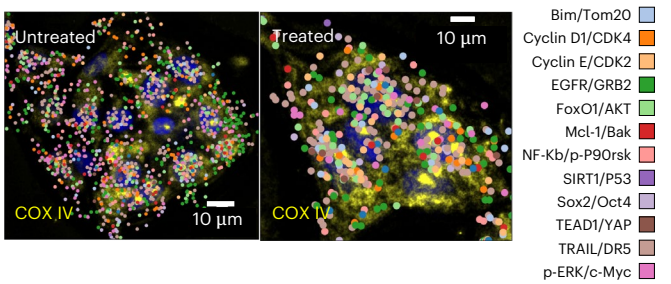

networks. We observed increased regulation of p-ERK/c-Myc PPI activity after osimertinib treatment in motif 9 (p-ERK/c-Myc and p-ERK/c-Myc), and the PPI of p-ERK/c-Myc occupies a large proportion in the network (Supplementary Fig. 32a and Dataset 17), which suggests that p-ERK/c-Myc may be the main effector of osimertinib. Also, more interactions between p-ERK/c-Myc and TEAD1/YAP were observed after treatment in a three-node motif 17 (Tead1/Yap and Tead1/Yap and p-ERK/c-Myc). This indicates that osimertinib may potentially increase the crosstalk between the ERK and YAP pathways. It has been found that with the combination of ERK and osimertinib treatment, the cells can still survive with upregulated YAP activity[4]. In the 9-PPI dataset, the autoregulation of cyclin D1/CDK2 in motif 0 and motif 45 was inhibited by osimertinib treatment (Supplementary Fig. 32b and Dataset 18), indicating suppressed cell cycle progression. Also, we observed downregulation of the interaction between sox2/oct4 and cyclin D1/CDK4 in both two-node (motif 2) and three-node interaction motifs (motif 47). Sox2 is highly expressed while repressing the expression of cyclin D1 in stem cells[50]. The reduced interactions may indicate the potential role of osimertinib in regulating stem-cell-like properties and cell proliferation. Dissecting the spatial networks into subgraph motifs reveals the organization of signalling networks. These small functional building blocks reflect that the interactions between PPIs are not random, which provides important clues to identify potential biomarkers for targeting signalling crosstalk.

To characterize the importance of subcellular spatial PPI event neighbourhood information and the number of PPI events detected, we benchmarked the performance of multiple machine learning and graph neural network models using 3D information (Fig. 4a) and compared the classification performance levels of drug responses on the basis of the number of detected PPI dots in the entire iseqPLA data (Fig. 4b). By processing all *z*-stack images in 3D, we captured all the PPI events across the *z*-dimension and combined them into a single PPI event by detecting the best focus plane and using a radius search algorithm (Methods and Supplementary Figs. 33 and 34). We compared the overall single-cell PPI event statistics between 2D and 3D information, verifying the reproducible distribution of the iseqPLA data (Supplementary Fig. 35 and Dataset 19).

The overall AUC score is higher when comparing the 13-PPI dataset with the 9-PPI and 5-PPI datasets. This better performance indicates the importance of a higher PPI target number for improving the separation of cell treatment state for the prediction pipeline (Fig. 4b). We also systematically compared the performance of 2D, 3D and 2D-3D fusion models, enabling a comprehensive evaluation of how varying levels of spatial data impact modelling at the cellular level (Fig. 4c). Our analysis revealed that in the highest-performing models—specifically the 9PPI-GraphConv, 13PPI-GCN and 13PPI-GAT—the 2D-3D fusion model demonstrated a notable improvement in cross-validated AUC scores compared with models utilizing either 2D or 3D data alone. This suggests that integrating multidimensional data can enhance model accuracy and robustness.

Moreover, it is important to note that the hyperparameters were originally tuned for the 3D models during the evaluation of the 2D-3D fusion model. This indicates that the overall performance of the 2D-3D fusion model could be further optimized by a comprehensive benchmarking of all relevant hyperparameters. In our methodology, the 2D-3D fusion was implemented through the concatenation of embeddings obtained post-graph pooling layer. Future research could explore alternative methods of domain fusion to more effectively integrate 2D and 3D information. Techniques such as early fusion, where data are combined at the initial stages, or late fusion, where final decisions are combined, could be investigated. In addition, advanced fusion strategies such as attention mechanisms or multitask learning could be applied to dynamically weight and integrate the complementary information from 2D and 3D domains, potentially leading to considerable improvements in model performance. Leveraging techniques such as multiple dropouts, Gaussian noise and *F*-correction[51] for feature selection using graph convolutional networks can further optimize model performance in high-dimensional, low-sample-size datasets, underscoring the importance of feature selection and model optimization in these contexts.

The total space and time complexity of the GNN model can be analysed by considering the operations performed in each layer across the entire network[52]. We demonstrated that as the number of layers and hidden layer size increase, the space and time complexity increases (Supplementary Fig. 36 and Dataset 20). The time and space complexity with respect to hidden layer size follows a quadratic trend, while time and space complexity with respect to the number of layers follows a linear trend.

Drug perturbing PPIs in EGFRm NSCLC cells

The study of the effect of osimertinib in NSCLC is limited to conventional approaches such as western blot and IF[53]. PPIs are potential drug targets and information on how osimertinib affects PPI expression levels is still lacking in the field. Osimertinib as the EGFR TKI can directly inhibit EGFR expression; however, it could also change the downstream signalling pathways by indirectly altering the baseline protein expression or the PPI expression. To investigate the PPI under direct drug perturbation, we demonstrated the effect of VP, a YAP/TEAD inhibitor, on YAP/TEAD1 interaction[7,8]. HCC827 cells were treated with 0, 1 and 10 μM for 24 h[54], and the cells were profiled with 2 cycles of Duolink PLA (YAP/TEAD1, EGFR/GRB2, TRAIL/DR5), followed by 2 cycles of Navinci (Sox2/Oct4, epithelial cadherins (E-cadherin)/β-catenin) and cell phenotyping markers (phalloidin, p-EGFR and Ki67) (Fig. 5a,b and Supplementary Table 3). Navinci is another PPI detection approach based on PLA. We demonstrated the compatibility of Duolink PLA and Navinci in iseqPLA. Nuclease P1 was used to remove probes. The overall PPI counts of YAP/TEAD1 between untreated and 1 μM treated cells were similar (Fig. 5c). Cells treated with 10 μM had an increased total number of YAP/TEAD1 dots (Fig. 5c and Extended Data Fig. 5a); however, fewer YAP/TEAD1 PPI dots occurred in the nucleus, with a lower nucleus ratio (Fig. 5d). Nuclei ratio was calculated on the basis of the ratio of PPI counts in the nucleus to the total PPIs per cell. YAP can translocate to the nucleus to activate TEAD transcription, and VP can induce the translocation of YAP1 and TEAD4 from the nucleus to the cytoplasm[55–57]. Our results demonstrated the effect of VP on the translocation of YAP/TEAD1 in HCC827 cells. Ki67 density, a new image-based morphological indicator, was also quantified by dividing the ki67 positive regions in the nucleus by the nuclear size (Extended Data Fig. 5b). We did not observe a decrease in ki67 density after drug treatment; however, the cell density was lower in 10 μM treated samples compared with both 1 μM and untreated cells. VP, the first small molecular inhibitor of YAP, can inhibit tumour proliferation and YAP activity. However, it is also limited by poor solubility and stability, and can result in Hippo-independent effects[58,59]. Since E-cadherin/β-catenin displayed an IF-like phenotype, we further quantified its mean intensity (Fig. 5c). E-cadherin/β-catenin functions in maintaining cell–cell contact, and the loss of E-cadherin facilitates the development of epithelial mesenchymal transition[60]. VP increased E-cadherin/β-catenin PPI counts (Fig. 5c), potentially promoting cell–cell contact. Nevertheless, the mechanism by which VP influences other PPIs within EGFR-related pathways remains elusive. Further studies are required to elucidate whether VP can serve as a potential therapeutic target.

Multiple PLA assays generate 47-plex protein profiles

To explore more PPI detection approaches other than Duolink PLA, we multiplexed 5 PPIs (Sox2/Oct4, E-cadherin/β-catenin, cell division cycle-25C (Cdc25c)/p38, proline-rich tyrosine kinase 2 (PYK2)/proto-oncogene c-Src (SRC), phosphor-Janus kinase (p-Jak2)/signal transducer and activator of transcription 3 (Stat3)), followed by cell phenotyping (phalloidin, p-EGFR and Ki67) in HCC827 cells treated with

https://doi.org/10.1038/s41551-024-01271-x

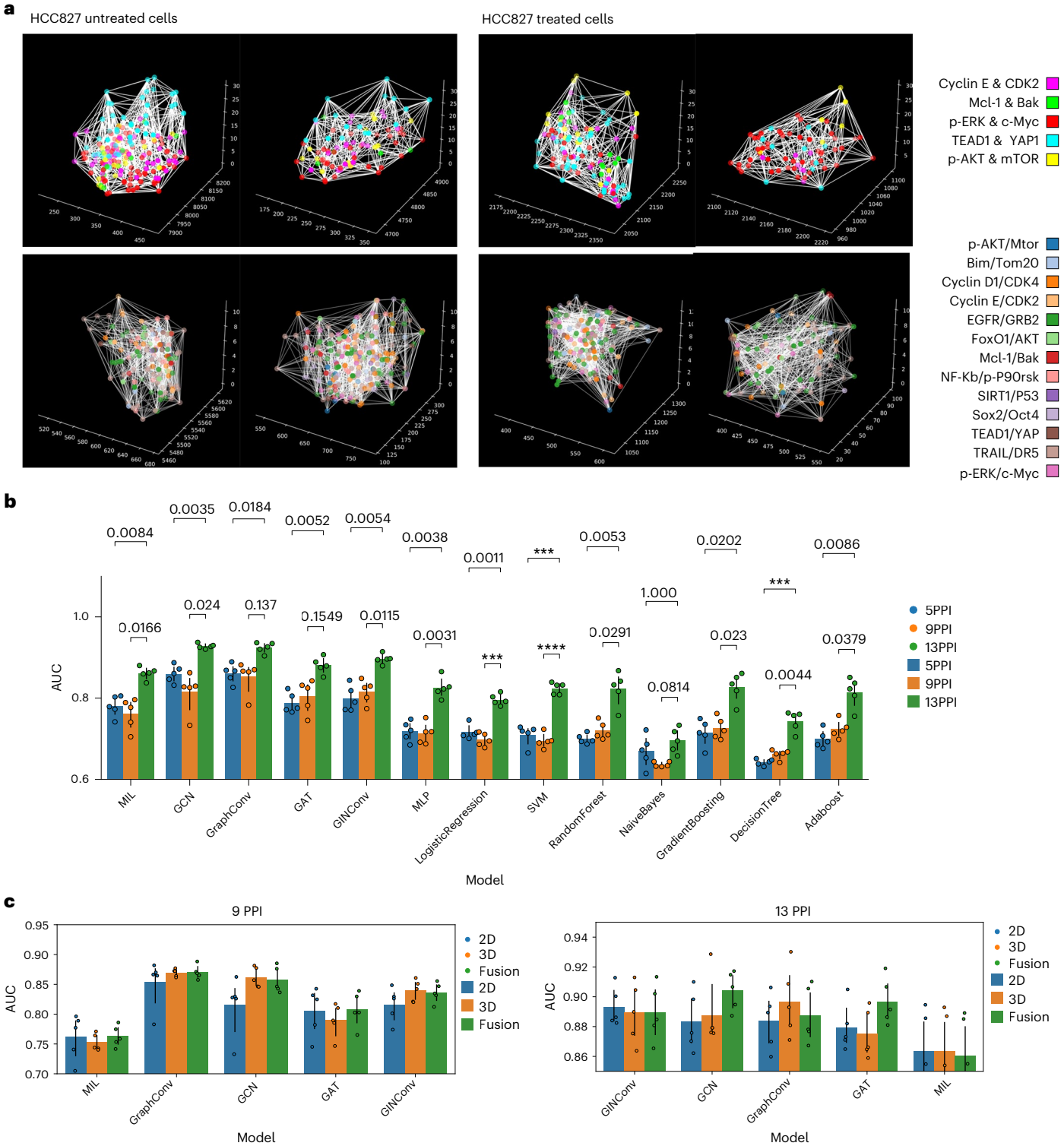

Fig. 4 | Predictive models in 2D and 3D of 5, 9 and 13 PPIs in HCC827 cells. **a**, 3D PPI spatial graph network representations at the single-cell level in HCC827 cells of 5 PPIs (top) and 13 PPIs (bottom). Axes labels indicate coordinates (x-y-z) of individual PPIs in pixel units. The colour of the node corresponds to the PPI type, and white edges correspond to the neighbouring node using Delaunay triangulation. **b**, Comparison of spPPI-GNN AUC scores across the 5, 9 and 13-PPI datasets. The 13-PPI dataset showed better prediction AUC scores than the 9 and 5-PPI datasets. Statistical testing was performed using independent-samples *t*-test with Bonferroni correction (***$0.0001 < P \leq 0.001$, ****$P \leq 0.0001$). **c**, Comparison of predictive model performance between the 2D PPI model, 3D PPI model and 2D-3D fusion model for 9 (left graph) and 13 (right graph) PPI dataset. Bar graphs are mean ± 95% CI.

and without 100 nM osimertinib for 12 h using the Navinci approach (Fig. 6a,b). Nuclease P1 was used to remove probes. We explored PPI involved in the calcium influx[61]. Calcium homoeostasis regulates cell proliferation, migration and cancer. Studying PPI events related to calcium influx can reveal potential therapeutic targets. PYK2 can sense calcium influx, and the binding of Src to PYK2 primes the phosphorylation of PYK2 and subsequent downstream signalling activation such as cell migration[62–64]. However, studies on the effect of osimertinib in

https://doi.org/10.1038/s41551-024-01271-x

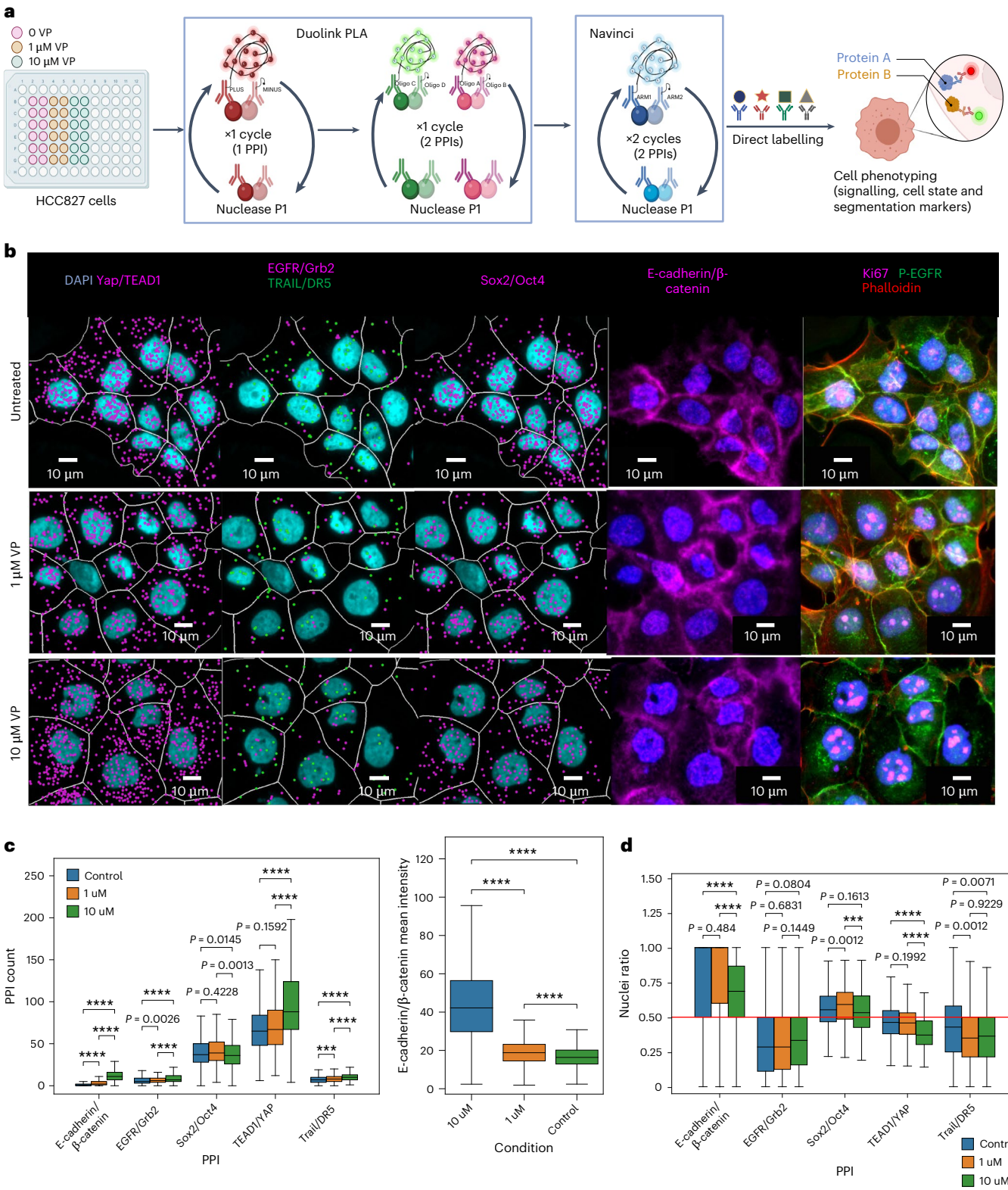

Fig. 5 | Evaluation of drug perturbing PPIs using VP drug in HCC827 cells. **a**, Schematic illustration of Duolink PLA and Navinci on HCC827 cells. HCC827 cells with 1 μM and 10 μM VP treatment for 24 h were stained with 2 cycles of Duolink PLA and 2 cycles of Navinci, followed by cell phenotyping. Created with BioRender.com. **b**, Visualization of 5 PPIs represented in scatter dots overlaid with DAPI. The white boundary is a combined mask from phalloidin and p-EGFR. The total cell numbers are 496, 574 and 265 for untreated, 1 μM and 10 μM treated cells. **c**, Left: comparison of PPI counts between VP-treated and unteated HCC827 cells. Right: mean intensity of E-cadherin/β-catenin. The separate PPI counts comparison in cytosol and nuclei is shown in Extended Data Fig. 5a. **d**, Comparison of nuclei ratio of PPI counts between VP-treated and unteated HCC827 cells. The nuclei ratio was calculated on the basis of the ratio of PPI counts in the nucleus to the total PPIs per cell. The red line indicates where the nuclei ratio equals 0.5. Statistical testing was performed using two-sided Mann–Whitney Wilcoxon test (***$0.0001 < P \leq 0.001$, ****$P \leq 0.0001$). Box plots in **c** and **d**: median (horizontal line inside box), 25th and 75th percentiles (box), 25th and 75th percentiles ±1.5 times the interquartile range (whiskers).

PYK2/Src are still lacking. Another pair of PPIs involved in cell migration is E-cadherin/β-catenin. Since the E-cadherin/β-catenin PPI events were too dense, we quantified the PPI events by calculating their mean intensity. Osimertinib inhibits the interaction between E-cadherin and β-catenin (Fig. 6c). Jak/STAT3 is another downstream pathway of EGFR. p-Jak2 (Y1007 + Y1008) can phosphorylate and activate STAT3, resulting in the activation of the JAK/STAT3 pathway[65]. The constitutive activation of the JAK/STAT3 pathway plays an important role in priming cancer development[66]. Osimertinib increased the p-Jak/Stat3 interactions (Fig. 6c). P38 could inhibit Cdc25c through direct phosphorylation, resulting in cell cycle arrest in G2 (ref. 67). The increase in Cdc25c/p38 PPI counts indicates the potential role of osimertinib in promoting cell cycle arrest (Fig. 6c). Sox2/Oct4, a common pair between Navinci and Duolink PLA, exhibited similar downregulation after osimertinib treatment (Fig. 6c). Cells treated with osimertinib displayed decreased ki67 density compared with untreated cells (Extended Data Fig. 5c).

The capability to integrate Duolink PLA with Navinci was demonstrated in HCC827 cells treated with the VP drug (Fig. 5). To explore indirect PLA on cell cultures, HCC827 cells treated with and without osimertinib were incubated with 5 pairs of primary antibodies in 1 cycle, each containing one anti-rabbit and one anti-mouse antibody. The combined 5-PPI profiles were obtained using anti-rabbit and anti-mouse secondary antibodies conjugated to PLUS/MINUS probes (Fig. 6d,e). Nuclease P1 effectively removed PLUS/MINUS probes. The cdc25c/p38 PPI events were decreased after osimertinib (Fig. 6f). The secondary antibodies from the indirect Duolink PLA may interfere with the binding of cdc25c and p38 primary antibodies. Thus, the order of direct and indirect PLA may need to be optimized within iseqPLA. To calculate the PPI signal more accurately, we further quantified the mean pixel intensity of the combined 5-PPI events by dividing the total pixel intensity by the total number of dots (Fig. 6f). By combining Navinci and Duolink direct and indirect PLA, the PPI panels could be expanded from 13 to 22 PPIs, comprising a total of 44 protein profiles that include 13 Duolink direct PPIs, 5 Duolink indirect PPIs and 4 Navinci PPIs. Following iseqPLA, cell phenotypes can be resolved using phalloidin, p-EGFR and Ki67, achieving a 47-plex protein profile. Similar to fluorescence in situ hybridization of cellular heterogeneity and gene expression programmes (FISHnCHIPs), which can image ~2–35 co-expressed genes in tissues simultaneously[68], indirect PLA enables the profiling of a group of proteins with similar functions concurrently, resulting in co-localized spatial expression patterns. Abnova Corporation offers 594 pairs for PPIs, enabling us to achieve a 1,000-plex protein profiling capability.

Spatial-signalling PPI networks in lung cancer tissues

To verify the feasibility of detecting PPIs in situ, we investigated iseqPLA on HCC827-derived mouse xenografts (CDX). The iseqPLA on cell culture resolves the PPI at the subcellular level; however, it fails to consider the architecture of cellular distributions. Our study utilized iseqPLA on the tissue to generate single-cell signalling maps within the context of the tumour microenvironment.

HCC827-derived xenografts in mice were treated with and without osimertinib for a sustained period, and OCT sections were obtained to compare the emergence of resistance. Osimertinib was given to mice daily. HCC827 xenografts in mice receiving osimertinib treatment were effectively inhibited for the first week. The tumour almost disappeared after a 5-day osimertinib treatment. As treatment continued, the tumour grew back and larger, indicating the development of acquired resistance to osimertinib. Therefore, in our study, iseqPLA was performed on mouse HCC827-cell-derived xenograft tissues in the presence of osimertinib treatment for 1 week and 2 months, representing responders and non-responders. We detected the dynamics of 5 PPIs related to organelle localization, proliferation markers and gene expression (Fig. 7a and Supplementary Fig. 37). Between cycles, nuclease P1 was used to remove probes. Pan-cytokeratin (panCK) was utilized to help differentiate tumour regions. The nearest-pixel method was utilized to assign PPI signals to the nearest cell with incomplete cell segmented regions (Fig. 7b). We found that osimertinib enhanced p-ERK/c-Myc while downregulating p-AKT/mTOR PPIs after the 2-month treatment (Fig. 7c). This indicates that mice became less sensitive to osimertinib and even developed acquired resistance to osimertinib, functioning as non-responders after the 2-month treatment (Fig. 7c, Supplementary Fig. 38 and Dataset 21). Also, mouse tissues treated with osimertinib for 2 months expressed more panCK-positive cells. The downregulation of cyclin E/CDK2 in 1-week osimertinib-treated mice also indicates inhibited cell cycle progression (Fig. 7c).

A spatial network was used to visualize the PPI distributions at the single-cell level in the mouse xenograft tissues (Fig. 7d). Similarly to other benchmarks, we compared the overall model performance in determining the overall treatment condition of tumour cells by looking at the pan-cytokeratin staining (Methods and Fig. 7e). That is, from IF staining, we classified cells expressing pan-cytokeratin-positive cells and filtered out all cells not expressing pan-cytokeratin staining. Next, we used spPPI-GNN to predict the treatment length between the spatial PPI networks extracted from those pan-cytokeratin-positive cells. The spPPI-GNN model outperformed other benchmarked models for predicting the treatment state at the single-cell level from human tissues.

To investigate the clinical relevance of our spatial-signalling interactomics approach, we performed iseqPLA on patient tissues with EGFRm NSCLC osimertinib responder and non-responder cells including 2 cycles of multicolour (Sox2/Oct4, NF-κB/p-P90rsk, cyclin D1/CDK4, TRAIL/DR5) and 1 cycle of single-colour (cyclin E/CDK2) detection, followed by immunofluorescence staining to phenotype immune cells (Cluster of differentiation 20 (CD20), Clusters of differentiation 4 (CD4), Clusters of differentiation 8 (CD8)), tumour cells (panCK) and cell boundary (phalloidin, Concanavalin A, WGA) (Fig. 8a and Supplementary Fig. 39a). Between cycles, nuclease P1 effectively removed the probes. Sox2/Oct4 PPI was upregulated in patients who responded to osimertinib treatment (Supplementary Fig. 39b and Dataset 22). Integrating both IF and haematoxylin and eosin (H&E) images of responder tissue at the single-cell level, we identified stroma, tumour and immune regions, and quantified the PPI events per cell in these regions (Methods, Fig. 8b,c and Supplementary Fig. 39c). The cell type distributions were further visualized using spatial neighbourhood maps in responder tissue (Fig. 8c and Supplementary Fig. 40a–c). Each

Fig. 6 | Multiple PLA assays generated 47-plex protein profiles in HCC827 cells. a, Schematic illustration of the workflow for 13-plex iseqPLA. HCC827 cells with and without 12-h 100-nM osimertinib treatment were stained with 5 cycles of Navinci PLA, followed by cell phenotyping (phalloidin, p-EGFR and Ki67). Created with BioRender.com. **b**, Visualization of 5 PPIs represented in scatter dots overlaid with DAPI. The white boundary is a combined mask from phalloidin and p-EGFR. The total cell numbers are 742 and 506 for untreated and osimertinib-treated cells, respectively. **c**, Left: comparison of PPI counts between osimertinib-treated and untreated HCC827 cells. Right: mean intensity of E-cadherin/β-catenin. **d**, Schematic illustration of the workflow for 15-plex iseqPLA. HCC827 cells with and without 12-h 100-nM osimertinib treatment were stained with 1 cycle of Duolink indirect PLA containing 5 PPIs, followed by 1 cycle of Navinci and then cell phenotyping (phalloidin). Created with BioRender.com. **e**, Visualization of combined 5 PPIs and 1 Navinci PPI represented in scatter dots overlaid with DAPI. The white boundary is a mask from phalloidin. The total cell numbers are 612 and 615 for untreated and osimertinib-treated cells, respectively. **f**, Left: quantification of 2 cycles of PPIs per cell between treated and untreated HCC827 cells. Right: mean pixel intensity of combined 5 pairs in untreated and treated HCC827 cells. The mean pixel intensity was calculated by dividing the total pixel intensity by the total number of dots at the single-cell level. Statistical testing was performed using two-sided Mann–Whitney Wilcoxon test (****$P \leq 0.0001$). Box plots: median (horizontal line inside box), 25th and 75th percentiles (box), 25th and 75th percentiles ±1.5 times the interquartile range (whiskers).

https://doi.org/10.1038/s41551-024-01271-x

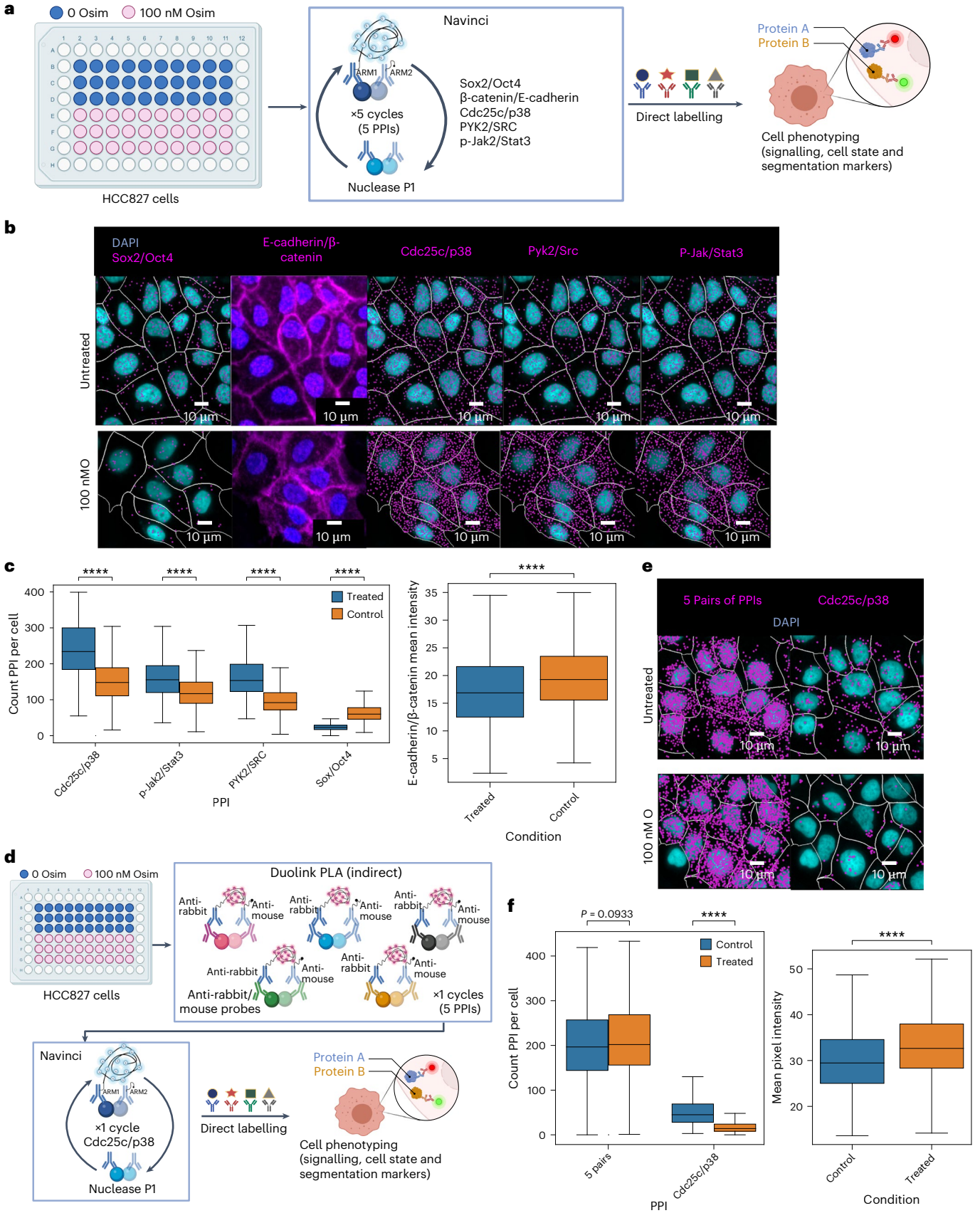

https://doi.org/10.1038/s41551-024-01271-x

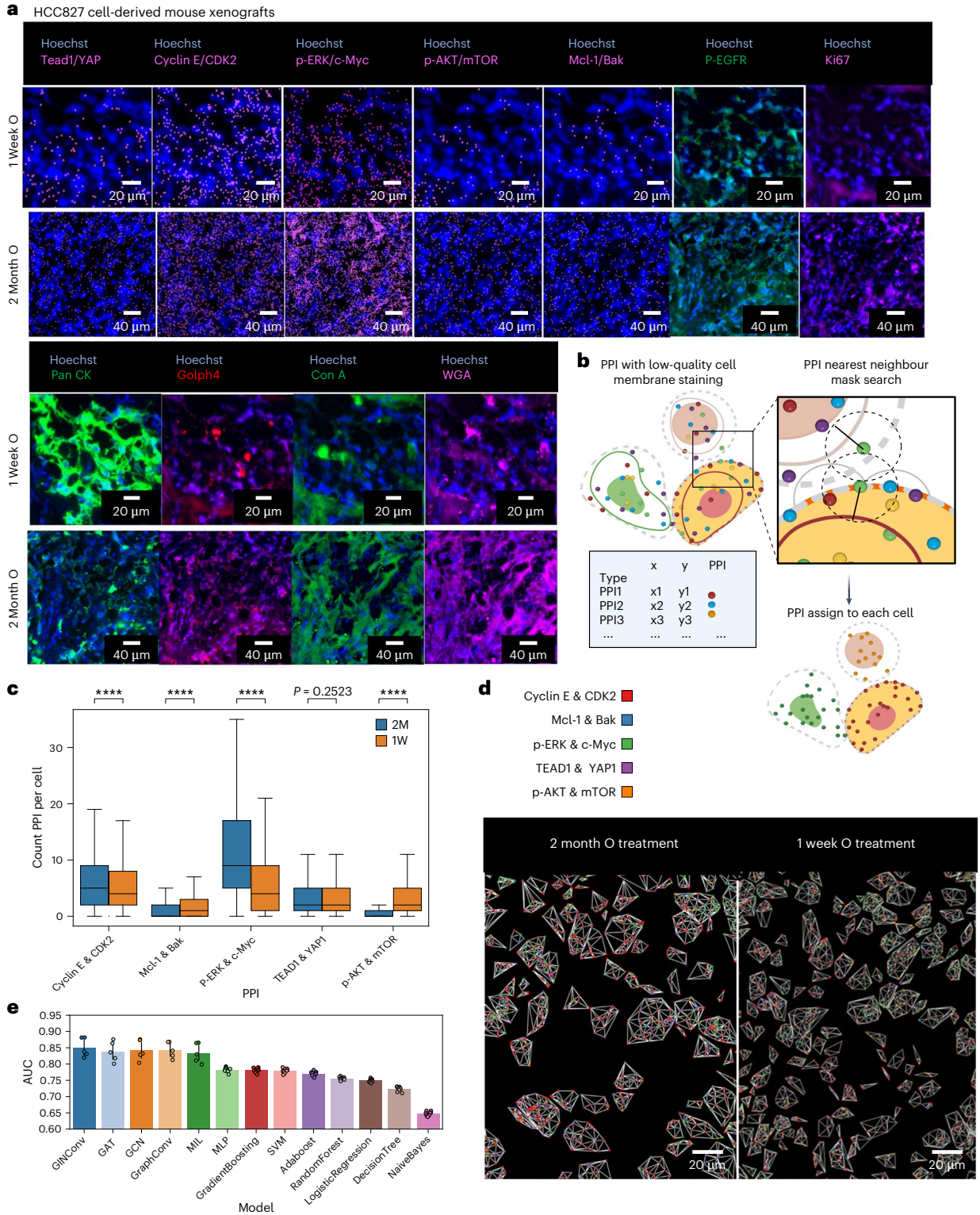

Fig. 7 | Quantification and modelling of 16-plex profiling for 5 PPIs and 6 organelle signalling markers in HCC827-cell-derived mouse xenografts. **a**, Visualization of 5 PPIs represented in scatter dots followed by 6-protein IF staining in HCC827-cell-derived mouse xenografts, treated with osimertinib for 1 week and 2 months separately. Seven panels demonstrate 5 pairs of PPIs and two IF markers (p-EGFR and Ki67) in the top two rows, and the subsequent four panels indicate four IF markers (PanCK, Golph4, ConA (Concanavalin A) and WGA) in the bottom two rows. **b**, Schematic showing the nearest-pixel method for assigning PPI signals to the nearest cell with incomplete cell segmented regions. Created with BioRender.com. **c**, PPI quantification comparison in pan-cytokeratin-positive regions between mice treated with osimertinib for 1 week and 2 months. Separate comparison of PPI counts in pan-cytokeratin-positive regions in cytosol and nuclei is shown in Supplementary Fig. 38. The total cell numbers are 18,429 and 25,790 for 1-week and 2-month osimertinib-treated tissues. Statistical testing was performed using two-sided Mann–Whitney Wilcoxon test (****$P \leq 0.0001$). **d**, Illustration of the PPI network in tissues at the subcellular level in two FOVs. **e**, Comparison of AUC scores between the spPPI-GNN, ML, MIL and MLP models for prediction of single-cell treatment status in the mouse xenograft dataset. GCN and GINConv layer-based spPPI-GNN show the best overall scores. Box plots in **c**: median (horizontal line inside box), 25th and 75th percentiles (box), 25th and 75th percentiles ±1.5 times the interquartile range (whiskers). Bar graphs in **e**: mean ± 95% CI.

node in the neighbourhood map represents one cell. The colour of the node represents different cell types including stroma, immune, tumour and other cells. The neighbouring map was constructed using a radius search of 20 µm[69]. The PPI counts per cell in regions with and without immune neighbours in the responder tissue were also compared (Fig. 8d and Extended Data Fig. 6a). PPI counts per stromal or immune cell with immune neighbours did not display a significant difference; however, Sox2/Oct4 per tumour cell with no immune neighbours displayed slightly higher interactions (Fig. 8d and Extended Data Fig. 6a). Due to the low copy number of PPI events in FFPE tissues, we compared the PPI density in lymphocytes and tumour-enriched regions among the responder and non-responder tissues (Fig. 8e, Extended Data Fig. 6b and Supplementary Fig. 40d). The identification of lymphocytes and tumour-enriched regions was based on the H&E images. In the patient who developed resistance to osimertinib, there was a noticeable reduction in the Sox2/Oct4 interactions, accompanied by an upregulation of NF-kB/p-P90RSK interaction in the tumour-enriched regions (Fig. 8e). In addition, we observed an elevation in the TRAIL/DR5 PPI events in the lymphocyte-enriched regions of the non-responder tissue (Extended Data Fig. 6b). However, some regions in the non-responder biopsy tissue exhibited warping during the process of collection. To comprehensively understand the dynamics of these protein interactions, further investigations using high-quality clinical tissues and more tissue samples are needed.

To demonstrate the feasibility of detecting PPIs using a super-resolved microscope, we compared the iseqPLA detected by a widefield microscope vs a Zeiss 900A with an Airy scan. The negative control with one MINUS probe alone confirmed the validity of the iseqPLA protocol (Supplementary Fig. 41).

Discussion

We have shown an image-based multiplexing approach to detect PPI at the subcellular level. The iterative processes of ligation, amplification, imaging and DNase treatment allowed us to detect 9 PPIs in cell cultures and 5 PPIs in tissues. We evaluated sensitivity, specificity and batch consistency, as well as whether the drug affects protein baseline or PPI levels. We showed the feasibility of integrating iseqPLA with RapMIF to profile both PPIs and signalling, proliferation and organelle markers. The upregulation of Tead1/YAP and p-ERK/c-Myc PPIs after osimertinib treatment in HCC827 cells may indicate the activation of YAP and the p-ERK pathway as compensatory pathways to EGFR inhibition. The co-expression analysis evaluated the co-localization of signalling markers with organelles. Also, we observed that DNase interfered with phalloidin signalling in HCC827 cells. Therefore, a combination of p-EGFR, concanavalin A and WGA was used for cell segmentation. DNase digests both single-strand and double-strand DNA in the nucleus, suggesting that it may change the localization of proteins connected with DNA and reduce PPI detection in later cycles. To reduce the negative effect of DNase on PPI detection, we further conducted experiments examining the effects of nuclease P1 and DMSO stripping solution on deactivating oligos and fluorophores. Nuclease P1 and DMSO exhibited comparable effects on digesting DNA as DNase. Nuclease P1 targeting only single-strand DNA serves as a good alternative to nuclease P1. Also, it preserves decent staining of phalloidin, indicating that it has minimal effect on changing the localization and structure of proteins.

Various approaches have been employed to assess the specificity and sensitivity of PLA. Overall, PLA exhibited higher specificity and sensitivity than other immune-PCR and ELISA assays. The specificity is dependent on the quality of primary antibodies. If the antibody lacks specificity for the target, it may bind with the non-specific target, yielding false positives. Alternative sequencing-based protein identification approaches, such as chromatin immunoprecipitation followed by sequencing (ChIP-seq) and cellular indexing of transcriptomes and epitopes by sequencing (CITE-seq), can quantify both the transcription factors and proteins. However, the data quality relies on the antibodies used[70,71]. Also, CITE-seq is limited to tagging surface proteins[70]. Prox-seq combines PLA with single-cell sequencing, enabling the quantification of gene expression, protein expression and PPIs[18]. Despite its effectiveness, Prox-seq is an antibody-based approach, limiting its ability to available reagents and antibody quality. Therefore, implementing technical controls on the primary antibodies is essential. Also using monoclonal antibodies as primary antibodies can greatly enhance sensitivity and specificity[72]. In addition, several factors such as cell seeding density, cell number and the heterogeneity of single cells may influence the PPI counts.

To better incorporate spatial information into our predictive model, we transformed our single-cell PPI events into graphs and developed spPPI-GNN, a predictive pipeline for determining the drug treatment outcome from single-cell PPI data. We benchmarked our spPPI-GNN predictive pipeline using spatial PPI graphs with ML, MLP and MIL models, and showed that spatial information plays an important role in improving the prediction of single-cell states. We also showed that 3D graphs of PPI resulted in better cell-state predictive abilities compared with 2D graphs of PPI, while the 2D-3D fusion models could enhance the AUC compared to 3D data only.

Moreover, we tested the scalability of our spPPI-GNN model by applying it to various data types such as cell culture, mouse xenograft and patient tissues with various numbers of PPI targets. Moreover, we benchmarked the ability of spPPI-GNN to predict cell surface proximity data on the basis of the protein count with a higher number of features (more than 1,000)[73]. We tested our spPPI-GNN algorithm on a cell surface protein detection assay[73] (Supplementary Fig. 42). This assay is a DNA-sequencing-based method for single-cell analysis to quantify protein abundance and spatial proximity at the cell surface using antibody oligonucleotide conjugates. The 3D spatial co-localization of protein abundance is represented in 3D spherical coordinates. To visualize the Pixelgen data, we extracted the 3D surface neighbouring information by using a 3D spherical surface Delaunay

Fig. 8 | Quantification of 17-plex profiling for 5 PPIs and 7 organelle signalling markers in patients with EGFRm NSCLC. a, Schematic illustration of the workflow for 17-plex iseqPLA. One responder and one non-responder patient tissues were stained with 5 cycles of PLA, followed by cell phenotyping including immune, tumour, signalling and segmentation markers. Created with BioRender.com. **b**, Quantification of PPI counts per cell in the stroma, tumour and immune regions in the responder tissue. The total cell numbers are 188, 884 and 1,614 in the immune, stroma and tumour regions, respectively. Statistical testing was performed using independent-samples *t*-test with Bonferroni correction (****$P \leq 0.0001$). **c**, Illustrations of H&E image overlaid with 5 PPIs (top left), H&E image overlaid with cell type masks (top right), the PPI event scatter dots with cell boundary (bottom left) and spatial neighbourhood maps of cell types constructed using a 20 µm radius (bottom right). Each node in the neighbourhood map represents one cell. The colour of the node represents different cell types including stroma, immune, tumour and other cells. Example images of a larger FOV are shown in Supplementary Fig. 40. **d**, Quantification of PPI counts for tumour cells with and without immune cell neighbours in the responder tissue. The total cell numbers are 318 and 1,296 in the regions with and without immune cell neighbours. Statistical testing was performed using independent-samples *t*-test with Bonferroni correction. **e**, Left: comparison of the density of PPI counts in tumour-enriched regions between responders and non-responders. Right: example images of 5 PPIs expression in tumour-enriched regions. Col 1: visualization of 5 PPIs in tumour-enriched regions. Col 2: distributions of Sox2/Oct4 PPI in red. Col 3: distributions of NF-kB/p-P90RSK PPIs in green. A comparison of the density of PPI counts in lymphocyte-enriched regions is shown in Extended Data Fig. 6b. The total cell numbers are 19 in the selected regions of both non-responder and responder tissues. Statistical testing was performed using independent-samples *t*-test (****$P \leq 0.0001$). Box plots and violin plots: median (horizontal line inside box), 25th and 75th percentiles (box), 25th and 75th percentiles ±1.5 times the interquartile range (whiskers).

https://doi.org/10.1038/s41551-024-01271-x

triangulation algorithm from control and stimulated T cells (Supplementary Fig. 42a and Dataset 23). Each node corresponds to an area of the cell surface where multiple protein targets are quantified. We have shown examples of the normalized protein count for HLA-ABC, CD45 and CD8 markers. We benchmarked the overall prediction of T-cell states and showed better AUC scores when using spPPI-GNN and the corresponding 3D graph representation. The nature of graph-based learning from the spPPI-GNN data allows the scaling of application of the pipeline to multiple high-plex spatial omics data sources, such as subcellular RNA FISH imaging or cell-level spatial transcriptomic imaging, and various prediction tasks such as treatment response or state predictions. One limitation of this pipeline is the dependence on high-quality data and event detection that might lead to batch effect during the pipeline. Moreover, it is difficult to combine various data

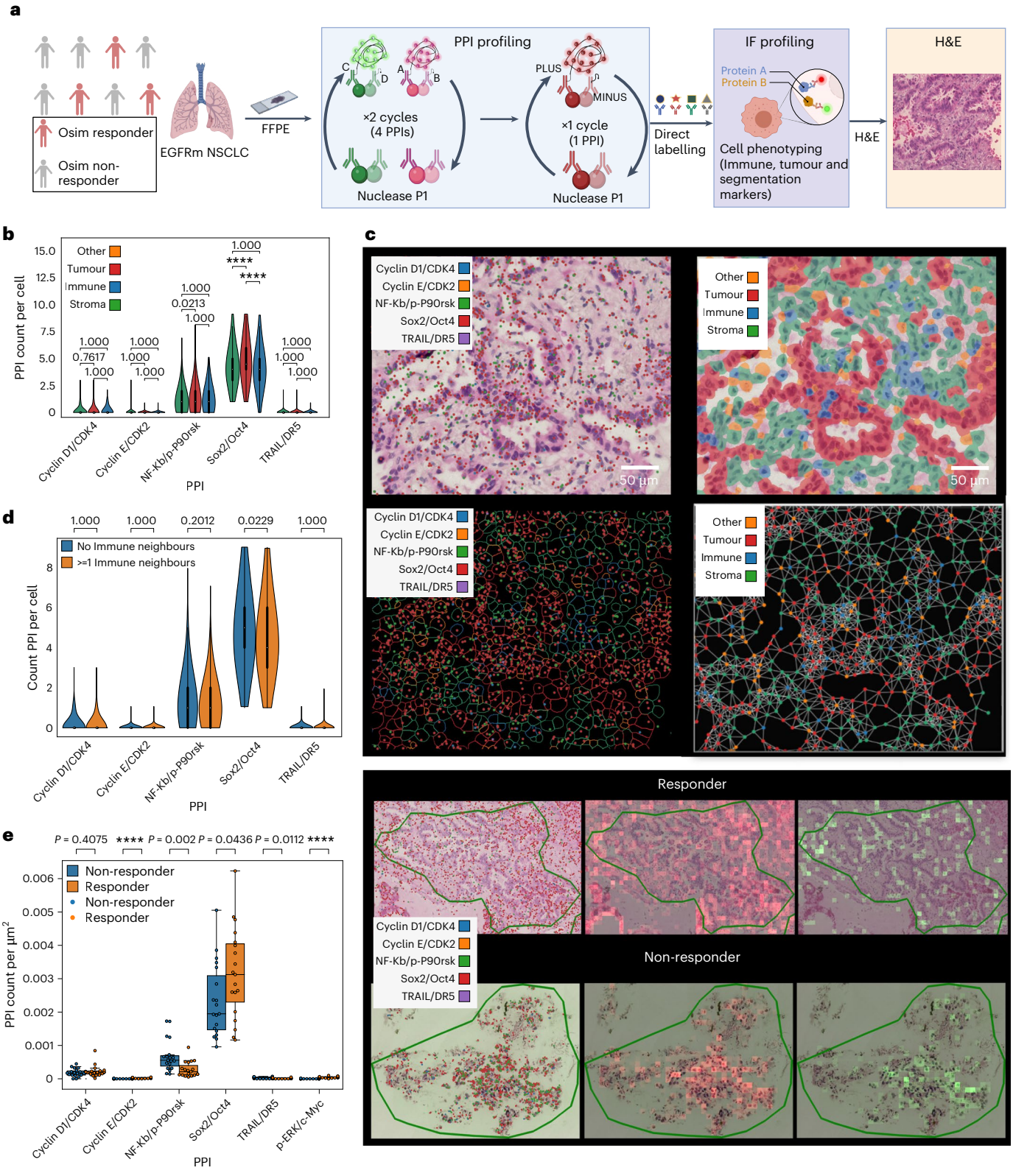

modalities as well as unseen or unmatching feature sets. Despite these limitations, spPPI-GNN is a unique pipeline for predicting cell-level state using subcellular level spatial information, providing an analysis beyond raw count difference analysis.

To select the PPI of interest, a bioluminescence resonance energy transfer (BRET)-based differential PPI discovery platform can be performed to reveal the differential interactions between wild-type NSCLC and EGFRm NSCLC cells. This quantitative high-throughput PPI screening platform can detect direct PPI with a proximity of <10 nm[74]. By comparing the PPI between wild-type and mutant cells, novel mutation-directed PPIs that function in potential alternative signalling pathways can be discovered. The selected PPIs are involved in the EGFRm-related signalling pathways. The selection includes the upstream, downstream and effectors in the AKT/mTOR, ERK/MEK and YAP/TEAD1 pathways. They not only indicate the activity of the signalling pathway, but they also demonstrate the cell response including cell proliferation and apoptosis in response to drug perturbations. The selection of PPIs in our panel is based on literature review, the OncoPPi and Bioplex interactome networks.

Another method to determine potential PPIs is to prescreen interesting pairs using affinity-purification mass spectrometry. The underlying bait–prey pairs can be selectively purified and quantified by mass-spectrometry analysis. This can help us determine the interactome of target proteins between mutant and wide-type cells to understand the EGFRm-resistant mechanisms. The potential target proteins include p-AKT, ERK and YAP. Owing to the unknown biological questions involved in the signalling cascades, it is hard to determine one pair of proteins that do not interact with each other at all. To examine the specificity of iseqPLA, we could use protein knockout as our negative control.

There are emerging PPI assays and technologies, including co-IP[75,76], PROPER-seq[77], pull-down assays[78,79], yeast two-hybrid (Y2H)[80,81], far-western blotting[82], tandem mass spectrometry[83], protein microarray[84], APEX[85,86], BioID[87], TurboID[88], FRET[89], BRET[90] and OncoPPI[74]. However, most of them are limited to bulk level or by the degree of scalability. The conventional PPI-detection approaches using MS cause the loss of spatial information owing to the sample-preparation step and to peptide extraction[91]. Unlike Co-IP, PLA preserves the spatial information of proteins without cell lysis and can be performed on both cell cultures and tissues. The efficiency of detection can be improved using UnFold probes, which prevent the cross-reactive detection of irrelevant proteins using a hairpin loop structure[14]. Via iseqPLA, the sequential imaging and labelling of PPIs allow for the large-scale profiling of protein interactions at the single-cell level.

In summary, iseqPLA illustrates the feasibility of multiplexing PLA and detecting multiple PPI distributions at the subcellular level. It also shows the value of modelling drug-treatment outcomes with graph-based PPI inputs, which integrates both the quantification and spatial information of protein interactions. This predictive model would predict treatment outcomes via signalling-network inputs and overcome the limitation of a lack of spatial details when using bulk-signalling assays.

Methods

Cells

A549 cells were used for antibody optimization. The cells were seeded on coverslips treated with 0.01% poly-L-lysine in a 6-well plate overnight in a 37 °C incubator. A549 was purchased from ATCC. NSCLC-sensitive cell line, HCC827 was provided by Dr Sun Shi-yong (Emory University). HCC827 cells were seeded on coverslips in a 6-well plate overnight, followed by osimertinib treatment.

Drugs

Osimertinib was provided by Dr Sun Shi-yong (Emory University) at 10 mM concentration. HCC827 cells were treated with 100 nM osimertinib at different time points in a 37 °C incubator. The cells were then fixed and permeabilized with 1.6% formaldehyde in 1×PBS for 10 min at r.t. and 0.5% Triton X-100 for 10 min at r.t., respectively. The cells were then blocked using a cell staining medium (CSM) containing 0.5% BSA and 0.02% sodium azide in PBS. The effect of osimertinib on p-ERK(T202/Y204) was assessed. HCC827 cells were stained with p-ERK overnight, followed by 1-h incubation of secondary antibodies at r.t. and 10 min DAPI staining. The cells were then imaged at ×40 magnification, and the intensity levels were analysed. For the multiplexing experiment, HCC827 cells were treated with 100 nM osimertinib for 12 h in a 37 °C incubator, followed by iseqPLA. The coverslip was mounted on an acrylic holder for multiple cycles of staining. Verteporfin was purchased from MCE at a 10 mM concentration. HCC827 cells were treated with 0, 1 and 10 μM VP for 24 h. Following fixation and permeabilization, the cells were profiled with iseqPLA. The corresponding PPI counts were quantified and compared.

Tissues

HCC827-derived mouse xenografts were provided by Dr Sun Shi-yong (Emory University). Animal studies were conducted with the approval of the Institutional Animal Care and Use Committee (PROTO201700718) of Emory University. The mice were treated with osimertinib for either 1 week or 2 months. Osimertinib was given to mice daily via oral gavage at 10 mg kg^{-1} dose. Mice were then euthanized and the tumour was embedded in OCT for sectioning. The OCT tissues were fixed in acetone, rehydrated, permeabilized in 0.4% Triton X-100 and blocked, ready for multiplexed experiments.

Patient tissues were collected from Emory University. The use of human specimens was approved by the Institutional Review Board of Emory University (IRB00098377). iseqPLA analysis was conducted on two distinct samples: a resection responder tissue, which demonstrated responsiveness to osimertinib as the primary treatment, and a biopsy non-responder tissue that exhibited no response to osimertinib as the initial line of treatment.

Antibodies

In our study, a total of 53 antibodies were used. Seventeen PPIs targeting the AKT/mTOR, MEK/ERK and YAP/TEAD1, JAK/STAT, senescence and calcium influx pathways including TEAD1 (12292BF, Cell Signaling Technology (CST)), YAP (ab172373, Abcam), cyclin E (sc-247, Santa Cruz Biotechnology), CDK2 (sc-6248, Santa Cruz), p-ERK (T202 + Y204) (ab242418, Abcam), c-Myc (5605BF, CST), p-AKT (Ser473) (4060BF, CST), mTOR (2983BF, CST), Mcl-1 (66157BF, CST), Bak (12105BF, CST), cyclin D1 (66467, CST), CDK4 (23972, CST), NF-κB p65 (69994SF, CST), p-p90RSK (Ser380) (11989BF, CST), Bim (26184SF, CST), Tom20 (sc-17764, Santa Cruz), Oct4 (ab240358, Abcam), Sox2 (ab243909, Abcam), p53 (46565SF, CST), SIRT1 (ab233398, Abcam), EGFR (26038SF, CST), Grb2 (ab227117, Abcam), FoxO1 (29336SF, CST), AKT (4691BF, CST), Trail (3219BF, CST), DR5 (ab251269, Abcam), p-JAK2 (Y1007 + Y1008) (AB219728, Abcam), Stat3 (AB171359, Abcam), Cdc25c (AB232553, Abcam), p38 (9212BF, CST), E-cadherin (96743SF, CST), β-catenin (ab196204, Abcam), Pyk2 (AB228477, Abcam) and Src (AB269563, Abcam). Five PPIs were evaluated using indirect Duolink PLA: CDK4 (1:1,200) and CDKN1B (1:50) (Abnova DI0295); AKT1 (1:1,200) and SRC (1:50) (Abnova DI0453); FGFR1 (1:1,200) and PIK3R1 (1:50) (Abnova DI0315); CDC42 (1:1,200) and CASP3 (1:50) (Abnova DI0581); STK11 (1:1,200) and PRKAA2 (1:50) (Abnova DI0500). Ten protein markers were used for RapMIF, including p-EGFR (Y1068) (ab205827, Abcam), Tom20 (sc-17764, Santa Cruz), Ki67 (ab283699, Abcam), pan-cytokeratin (53-9003-82, Invitrogen), Golph4 (ab197595, Abcam), NBD-C6 (N22651, Thermofisher), Cox IV (ab197491, Abcam), phalloidin (A34055, ThermoFisher), wheat germ agglutinin (WGA, W32466, ThermoFisher) and Concanavalin A (C11252, ThermoFisher). For RapMIF, the antibodies were either purchased in preconjugated versions or conjugated with Alexa Fluor 488, 555 or 647 using the Lightning-Link Rapid Conjugation

kit (ab236553, ab269820, ab269823). For iseqPLA, the carrier-free antibodies were preconjugated with Duolink Probemaker (single colour: DUO92009 Sigma; multicolour: DUO96020 Sigma). Five PPIs (Sox2/Oct4, B-catenin/E-cadherin, Cdc25c/p38, PYK2/SRC, p-Jak2/Stat3) were conjugated to NaveniLink (NL.050). Before conjugation, the concentrations of the antibodies were measured using Nanodrop to ensure the required antibody amount was within the range. All antibodies involved in signalling pathways were first tested using IF in A549 cells. For unconjugated antibodies, IF testing was done overnight at 4 °C or at r.t. for 1 h. To improve the staining quality, titrations were performed on antibodies, and IF was evaluated at two different dilution rates. To optimize the antibody conditions, A549 cells were seeded on coverslips for antibody staining, followed by DAPI (62248, ThermoFisher). For IF staining on tissue, the antibodies and Hoechst 33342 (H3570, ThermoFisher) were diluted in a protein block buffer (DAKO, X0909).

iseqPLA on cell cultures

For single-colour detection, each coverslip prepared with cells was stained with multiple PPIs with one PPI per cycle. The cells were fixed and permeabilized, ready for the following staining steps: (1) blocking the sample with Duolink blocking solution; (2) incubating it with one pair of proteins, conjugated to one PLUS and one MINUS oligonucleotide at 4 °C overnight. The antibodies were diluted in Duolink antibody diluent at the preferred dilution rate; (3) incubating the sample with ligase for 30 min at 37 °C; (4) amplifying the signals for 100 min at 37 °C; and (5) staining the sample with DAPI. The sample was then ready for imaging.

For multicolour detection, after permeabilization, the cells underwent the following steps: (1) blocking the sample with Duolink blocking solution; (2) incubating it with two pairs of proteins, conjugated to one pair of oligonucleotides at 4 °C overnight. The antibodies were diluted in Duolink antibody diluent at the preferred dilution rate; (3) incubating the sample with ligase for 30 min at 37 °C; (4) amplifying the signals for 100 min at 37 °C; (5) incubating the sample with the detection buffer for 30 min at 37 °C; and(6) staining the sample with DAPI. The sample was then ready for imaging.

For indirect PLA, anti-rabbit and anti-mouse secondary antibodies conjugated to oligonucleotide PLUS/MINUS probes were used to target primary antibodies. After cell fixation and permeabilization, the cells were ready for the following steps: (1) blocking the sample with Duolink blocking solution; (2) incubating it with one pair of primary antibodies, one from rabbit and one from mouse. The antibodies were diluted in Duolink antibody diluent at the preferred dilution rate; (3) incubating the sample with anti-rabbit and anti-mouse secondary antibody PLUS/MINUS probes for 1 h at 37 °C; (4) incubating the sample with ligase for 30 min at 37 °C; (5) amplifying the signals for 100 min at 37 °C; and (6) staining the sample with DAPI. The sample was then ready for imaging. After imaging, the samples were incubated with DNase at a 1:50 dilution rate for 4 h at r.t., followed by 3× 30% formamide washes and 3× 1×PBS washes.

DNase

After acquiring the images of iseqPLA, the samples were incubated with DNase I (4716728001, Sigma) at a 1:50 dilution rate for 4 h at r.t., followed by 3× 30% formamide washes and 3× 1×PBS washes.

Navinci on cell cultures

The cells were fixed and permeabilized, ready for the following staining steps: (1) blocking the sample with Block NT; (2) incubating it with one pair of proteins, conjugated to one ARM 1 and one ARM 2 oligonucleotide at 4 °C overnight. The antibodies were diluted in Diluent 1 NT at the preferred dilution rate; (3) incubating the sample with Enzyme 1 NT in buffer 1 for 30 min at 37 °C; (4) incubating the sample with Enzyme 2 NT in buffer 2 for 90 min at 37 °C; and (5) staining the sample with DAPI. The sample was then ready for imaging.

iseqPLA on tissues

iseqPLA is compatible with tissues mounted on slides. The staining settings were the same as those for iseqPLA in cell cultures. We skipped the blocking step between cycles for tissue multiplexing to avoid hiding the signals. The tissue samples were mounted with 10% glycerol made in 1×PBS. We covered the slide using a 24 × 50 mm No. 1 coverslip (3322, Thermo Scientific) to prevent evaporation during imaging. To de-coverslip the sample after imaging, we placed the slide in a vertical jar containing 1×PBS for ~10 min, and the coverslip was released due to gravity.

RapMIF

Following iseqPLA, RapMIF was performed to profile pan-cytokeratin, ki67, Tom20, p-EGFR, Golph4, Bim, Concanavalin A, phalloidin and WGA. The settings were the same as those described previously[22]. Between cycles, the fluorophores were deactivated using a 3% H_2O_2 and 20 mM NaOH mixture made up in 1×PBS for 1 h at r.t. in the presence of white light, followed by 3× 1×PBS washes (for cell cultures: 3% H_2O_2 and 20 mM NaOH; for tissues: 4.5% H_2O_2 and 24 mM NaOH). For tissue multiplexing, after IF staining, we performed H&E staining at the last cycle.

Nuclease P1 stripping

Nuclease P1 was examined as an alternative to DNase I. Following the imaging of PPI, the samples were incubated with nuclease P1 for 30 min at 37 °C. The samples were then washed with 20 mM EDTA three times, followed by 3× 1×PBS washes.

H2 buffer

We added 30 ml of 5 M NaCl solution, 10 ml of 1 M Tris (pH 7.5), 0.943 ml of Triton X-100, 2.03 g of $MgCl_2{\cdot}6H_2O$ and 0.02% (w/v) NaN3 to 960 ml of double-distilled H_2O[36].

DMSO stripping solution

DMSO was also tested to remove oligos and PLA signals. Following the imaging of PPI, the samples were incubated with hybridization buffer (100 ml of DMSO with 400 ml of H2 buffer) for 1 min, followed by stripping buffer (62.5 ml of H2 buffer to 187.5 ml of DMSO) for 10 min at r.t. We then washed the samples three times with 1×PBS[36].

Imaging

A widefield microscope, Keyence BZ-X810, was used for fluorescence and brightfield imaging. The fluorescent signals were detected by five filters with an excitation spectrum of 360 nm (Alexa Fluor), 488 nm (FITC), 555 nm (TRITC), 590 nm (Texas red) and 647 nm (Cy5). The exposure time was varied, but the exposure time for each marker across control and drug-treated HCC827 cells was consistent. The sample of cells grown on the coverslip was imaged using a ×40 oil lens for multiple ROIs, and each ROI was imaged across 25–30 *z*-stacks with 0.4 µm per stack. The whole slide tissue was imaged using a ×20 dry lens, and each ROI was imaged using autofocus with a ×40 oil lens across 25–30 *z*-stacks with 0.4 µm per stack. The resolutions for the ×20 dry lens and ×40 oil lens were 0.37742 µm per pixel and 0.18872 µm per pixel, respectively.

Sensitivity

HCC827 cells were cultured and seeded on a 96-well plate, followed by no treatment or a 12-h osimertinib treatment at 5, 10, 25 and 100 nM. The cells were then fixed and ready for iseqPLA experiments. The cells were profiled with two cycles of iseqPLA (Cycle 1: Sox2/Oct4, p-p90RSK/NF-kB; Cycle 2: cyclin D1/CDK4, Bim/Tom20), followed by segmentation markers. Nuclease P1 was used to remove probes between cycles. The PPI counts were quantified.

Specificity

The HCC827AR/BimKO and HCC827AR/vector-only cells were cultured and seeded on a 96-well plate. The cells were then fixed using 1.6%

paraformaldehyde, ready for experiments. Following permeabilization and blocking, cells were stained with Bim/Tom20 and Sox2/Oct4 PPIs overnight. Following ligation, amplification and detection, the signals were imaged using a microscope. Cell phenotyping was performed using segmentation markers. Cells from the same batch were also stained with Bim using indirect IF. Quantification of PPI and IF staining of Bim antibody in cytosol and nucleus were performed.

HCC827 cells were stained with three cycles of PPI: anti-p-ERK PLUS probe only, anti-Yap MINUS probe only and cyclin E/CDK2 pair. Between cycles, the signals were removed using nuclease P1.

Baseline vs PPI

The HCC827 cells were cultured and seeded on a 96-well plate, followed by no treatment or a 12-h 100-nM osimertinib treatment. The cells were then fixed using 1.6% paraformaldehyde, ready for experiments. Due to the limitation that most of the antibodies used in the panel are from rabbit, we measured the protein baseline levels using indirect immunofluorescence on different wells. Subsequently, the corresponding PPI counts were measured using PLA. The cells were stained with segmentation markers (Concanavalin A, phalloidin and WGA) for cell mask identification.

Batch difference

HCC827 cells from two batches were cultured and seeded on the same 96-well plate, followed by no treatment or a 12-h 100-nM osimertinib treatment. The cells were then fixed, ready for iseqPLA experiments. The cells were profiled with two cycles of iseqPLA (Cycle 1: Sox2/Oct4, p-p90RSK/NF-kB; Cycle 2: cyclin D1/CDK4, Bim/Tom20), followed by segmentation markers. Nuclease P1 was used to remove probes between cycles. The PPI counts were quantified based on the cell mask.

Co-immunoprecipitation

The antibodies were first validated using western blot. HCC827 cells were treated with 100 nM osimertinib for 8 and 12 h, and then lysated for co-IP. C-Myc proteins were pulled down using c-Myc (CST, 9402S), followed by staining of p-ERK (CST, 9106S). Normal rabbit IgG (CST, 2729S) served as a negative control.

Luminex

HCC827 cells were lysed using Bio-Plex Cell Lysis kit (171304011) and stored at −80 °C. Cell lysate (1 µg) was diluted in assay buffer (provided in the multiplex assay) and analysed using the Milliplex MAP 9-Plex Multi-Pathway Magnetic Bead Signaling Kit Multiplex assay (Millipore Sigma, 48-680MAG). P-CREB, p-JNK, p-NFκB, p-p38, p-ERK1/2, p-Akt, p-p70S6K, p-STAT3 and p-STAT5 measurements were read using a MAGPIX Luminex instrument (Luminex).

Image processing

For 2D maximum projection images, we used stitched images provided by the BZ-X810 Analyser. We used the Hoechst channel from each cycle to register the images using a phase cross-correlation algorithm. For 3D per *z*-stack image processing, we stitched ROI images of 1,024 pixels by using a 30% overlap ratio, utilizing a code based on ASHLAR[92]. After stitching, we registered all cycle images per *z*-stack as the microscope captures each ROI *z*-stack image at once.

Cell segmentation

We used two distinct methods for single-cell segmentation of cell culture and tissue images. For cell culture images, we used the Cellpose[93] deep learning algorithm, whereas for tissue images we used the Mesmer[94] algorithm from the Deepcell[95] package for single-cell segmentation. Single cells in cell culture are more homogeneous with more defined cell boundaries, whereas cells in mouse tissue exhibited more variation in cell shape and size. We chose Cellpose for cell culture data and Mesmer for tissue data because the two algorithms were pretrained on corresponding data modalities. We used Hoechst for nuclei segmentation and p-EGFR as a cytosolic marker.

Cell phenotyping in tissue samples

HCC827-derived mouse xenograft cells were classified by the mean expression level of the pan-cytokeratin marker to differentiate cancer cells from normal mouse cells. Patient tissue sample cells were classified by combining IF phenotyping and an H&E cell classifier. We performed H&E staining at the last cycle in the patient tissue after IF staining. After registration and single-cell segmentation using the Deepcell algorithm, we first classified cells on the basis of their IF expression level. Cells expressing low staining for all markers were classified as 'others'. Next, using a pretrained Hover-Net model[96], we segmented and classified cells using H&E images into immune, stromal and cancer cells. Using the segmented cell centroids from H&E images, we matched each cell into the IF modalities and relabelled all 'other' class cells from the new H&E images. This allowed us to utilize the best available information from both the IF and H&E modalities.

PPI detection

PPI signals were detected using a custom algorithm leveraging a traditional image processing pipeline. More specifically, each PPI image was preprocessed as follows: images were first transformed using a top-hat filter of 3-pixel size to reduce the noise around PPI signals, then Laplacian of Gaussian images was used to detect bright local maxima as PPI signals. In 3D images, we filtered out double detection of PPIs at the same position in consecutive *z*-stacks. After detecting all the PPI locations in 3D, we looked at PPIs within a 2.5-pixel radius (0.045 µm) by creating a PPI neighbourhood graph of 2.5-pixel radius threshold and obtained all connected components in the graph. Finally, we extracted the mean position of the unique connected components in the graph as identified unique PPI signals in 3D. A 2.5-pixel radius was chosen empirically by comparing the number of PPIs detected as well as their spatial representation.

PPI cell assignment in tissue samples

In the mouse tissue data, the cell membrane segmentations do not capture the whole cell area. To avoid loss of PPI information due to cell segmentation error, we used a nearest-distance-based assignment method to assign the PPI signal detected that is not in any cell segmentation mask. For each PPI signal not in any segmented cell region, we looked at the nearest cell mask pixel; if the distance was lower than a user-defined value, we assigned it to the cell to which the nearest cell mask pixel belonged.

Spatial graph construction

For each detected PPI in a cell, we extracted the corresponding 2D or 3D localization and assigned a node in the created graph. The node labels were assigned by creating a one-hot encoding of the corresponding PPI detected for the node. Delaunay triangulation was used to create edges connecting the nodes in the graph and therefore create a PPI spatial graph for each cell. The models were trained in a multi-instance learning framework, that is, a cell label for each instance was assigned on the basis of the cell treatment condition of a group. For the cell-level spatial graphs, we used a radius search of 20 µm to determine neighbouring cells. That is, after single-cell segmentation, we calculated all cells within a 20 µm distance between their centroids and considered them as neighbouring cells.

SpPPI-GNN model. For the graph neural network, we used a multilayer network consisting of graph convolutional layers of 16–64 embedding size. The input of the model was the generated PPI graph for each cell with node feature represented by the PPI one-hot encoding. Each layer transformed the input as the following function: $H^{l+1} = f(W^l H^l A^*)$, where l is the corresponding layer, f is the activation function, H^l the node

embedding matrix, W^l the weight matrix of the layer l, and A^* the spectral normalized adjacency matrix. The spectral normalized adjacency matrix was obtained using the following formula: $A^* = D^{-\frac{1}{2}}AD^{\frac{1}{2}}$, where A is the corresponding adjacency matrix and D is the degree matrix of A. We benchmarked different graph layers' backbones (GCN[97], GAT[98], GINConv[99], GraphConv[100] and SAGEConv[101]) for optimal prediction in the validation set for 5-PPI, 9-PPI and 13-PPI data. Moreover, we benchmarked various hyperparameters for optimal parameter selection, such as the number of layers (2, 3 or 4) and the size of hidden layers (16, 32 or 64). The node embeddings were then aggregated by a pooling layer. Similarly, we benchmarked various pooling layers to investigate the best way of incorporating node-level features: mean, maximum, sum, global attention[102] and gated attention. Finally, two dense layers were then used to obtain prediction at the cell level (that is, graph-level prediction).

2D-3D fusion model

The 2D-3D fusion model utilized the 3D data in graph representation, with an edge characterizing the spatial distance between detected PPI events, and the corresponding maximum projected 2D data in graph representation, with an edge characterizing the spatial distance between PPI events projected on the same plane. To combine the 2D and 3D information, we used two spPPI-GNN models that took as input the 2D and 3D representations, respectively. We combined the graph-level embedding using concatenation or a tensor decomposition fusion module via Kronecker Product[103] with a gating-based attention mechanism[104] for cell-level prediction.

Multi-instance learning baseline

A multilayer perception baseline was used to compare our spPPI-GNN network. In the same multi-instance learning framework, we assigned a class label from the cell treatment condition. The input of the model was the generated PPI graph for each cell with node feature represented by the PPI one-hot encoding. Here we used stacked dense layers of embedding size 16 for the 5-PPI dataset and embedding size 32 for the 9-PPI dataset to obtain a node embedding. Each layer transformed the input as the following function: $H^{l+1} = f(W^l H^l)$, where l is the corresponding layer, f is the activation function, H^l the node embedding matrix and W^l the weight matrix of the layer l. Finally, the node embeddings were then aggregated by a pooling layer, and two dense layers were then used to obtain a prediction at the cell level (that is, graph-level prediction).

Machine learning baseline

Several machine learning models, including naïve Bayes, random forest, AdaBoost, decision tree, support vector machine (SVM) and gradient boosting, logistic regression and MLP, were used as a baseline on a total number of PPI events. We used the scikit-learn Python library with default setting when training and testing these machine learning models. We benchmarked these models using the total number of PPI events per whole cell (1) and divided by subcellular regions (2) (nuclei/cytosol). Therefore, the input is the sum of each PPI class in (1) the whole cell or divided by (2) cytosol and nuclei regions. The model output is the predicted treatment condition.

Complexity of GNN models

The total space and time complexity of the GNN model can be analysed by considering the operations performed in each layer across the entire network[52]. Each GNN layer involves three primary operations: feature transformation, neighbourhood aggregation and activation. For feature transformation, which involves a dense matrix multiplication between the node features and the weight matrix, the time complexity is $O(NF^2)$, where N is the number of nodes and F is the number of features per node. The neighbourhood aggregation step, which combines features from neighbouring nodes, has a time complexity of $O(N^2F)$ for dense graphs. The activation function applied element-wise to the node features adds a negligible time complexity of $O(NF)$. Thus, the total time complexity per layer for dense graphs is $O(NF^2 + N^2F)$, and for L layers, it becomes $O(LNF^2 + LN^2F)$. The space complexity includes storing the node features, weight matrices and the adjacency matrix. The node features require $O(NF)$ space, the weight matrix requires $O(F^2)$ space, and the dense adjacency matrix needs $O(N^2)$ space. Consequently, the space complexity per layer is $O(NF + F^2 + N^2)$, and for L layers, the total space complexity is $O(L(NF + F^2) + N^2)$.

To analyse the complexity of the GNN model, we calculated the time and space complexities using the formulas $LN^2F + LNF^2$ (time) and $N^2 + LF^2 + LNF$ (space). We varied L (number of layers) and F (hidden size) while keeping N constant at 90. For each combination of L and F, the complexities were computed and plotted. The graph illustrates how increasing the number of layers and features affects the computational steps and memory usage. Specific values of L and F were highlighted with markers to show their exact impact on the model's performance. We chose $N = 90$ because it is the mean number of nodes of the graphs in all datasets.

Pixelgen data

The data were collected from the Pixelgen database (https://software.pixelgen.com/datasets/cd20-rituximab-v1.0-immunology-I). Peripheral blood mononuclear cell samples were stimulated into phytohaemagglutinin (PHA) blasts with PHA-L, followed by 10 ng ml^{-1} of interleukin-2 for 5 days at 37 °C. The cells were added to plates coated with 5 µg ml^{-1} of human ICAM-1 (CD54) His-tag Fc Chimera Recombinant Protein (A42523) for 2 h. The aliquots of cells were treated with and without 10 ng ml^{-1} of regulated upon activation, normal T cell expressed and secreted (RANTES) or CCL5 at 37 °C for 1 h.

Prediction metrics. To compare the models' prediction abilities, we used a 5-fold cross-validation setting by separating the dataset into an 80% training set and a 20% validation set. We used the receiver operating characteristic AUC score as a metric to evaluate the data prediction in the validation sets.

Statistical testing. The details of statistical tests employed in each case are provided in the figure captions. All P values were corrected for multiple testing and the statistical testing method is indicated in the figure captions. We used the following convention to indicate significance with asterisks: ***($0.001 > P > 0.0001$) and ****($P \leq 0.0001$). Exact P values that are greater than 0.001 are shown on the plots.

Reporting summary

Further information on research design is available in the Nature Portfolio Reporting Summary linked to this article.

Data availability

The main data supporting the results of this study are available within the paper and its Supplementary Information. The statistics needed to recreate the figures are provided as Source Data. The raw data are available in figshare[105]. Source data are provided with this paper.

Code availability

The custom codes used in the study are available in GitHub[106].

References

1. Gu, J. et al. MEK or ERK inhibition effectively abrogates emergence of acquired osimertinib resistance in the treatment of EGFR-mutant lung cancers. *Cancer* **126**, 3788–3799 (2020).
2. Cheng, H. et al. Targeting the PI3K/AKT/mTOR pathway: potential for lung cancer treatment. *Lung Cancer Manage.* **3**, 67–75 (2014).
3. Xin, X. et al. CD147/EMMPRIN overexpression and prognosis in cancer: a systematic review and meta-analysis. *Sci. Rep.* **6**, 32804 (2016).

4. Kurppa, K. J. et al. Treatment-induced tumor dormancy through YAP-mediated transcriptional reprogramming of the apoptotic pathway. *Cancer Cell* **37**, 104–122.e12 (2020).
5. Ando, T. et al. EGFR regulates the Hippo pathway by promoting the tyrosine phosphorylation of MOB1. *Commun. Biol.* **4**, 1237 (2021).
6. Nguyen, C. D. K. & Yi, C. YAP/TAZ signaling and resistance to cancer therapy. *Trends Cancer* **5**, 283–296 (2019).
7. Wei, L. et al. Verteporfin reverses progestin resistance through YAP/TAZ-PI3K-Akt pathway in endometrial carcinoma. *Cell Death Discov.* **9**, 30 (2023).
8. Wei, C. & Li, X. Verteporfin inhibits cell proliferation and induces apoptosis in different subtypes of breast cancer cell lines without light activation. *BMC Cancer* **20**, 1042 (2020).
9. Kaushik, S. et al. A tyrosine kinase protein interaction map reveals targetable EGFR network oncogenesis in lung cancer. Preprint at *bioRxiv* https://doi.org/10.1101/2020.07.02.185173 (2020).
10. Lee, H.-W. et al. Profiling of protein–protein interactions via single-molecule techniques predicts the dependence of cancers on growth-factor receptors. *Nat. Biomed. Eng.* **2**, 239–253 (2018).
11. Rajapakse, H. E. et al. Time-resolved luminescence resonance energy transfer imaging of protein–protein interactions in living cells. *Proc. Natl Acad. Sci. USA* **107**, 13582–13587 (2010).
12. Maurel, D. et al. Cell-surface protein–protein interaction analysis with time-resolved FRET and snap-tag technologies: application to GPCR oligomerization. *Nat. Methods* **5**, 561–567 (2008).
13. Jalili, R., Horecka, J., Swartz, J. R., Davis, R. W. & Persson, H. H. J. Streamlined circular proximity ligation assay provides high stringency and compatibility with low-affinity antibodies. *Proc. Natl Acad. Sci. USA* **115**, E925–E933 (2018).
14. Klaesson, A. et al. Improved efficiency of in situ protein analysis by proximity ligation using UnFold probes. *Sci. Rep.* **8**, 5400 (2018).
15. Krieger, C. C., Boutin, A., Neumann, S. & Gershengorn, M. C. Proximity ligation assay to study TSH receptor homodimerization and crosstalk with IGF-1 receptors in human thyroid cells. *Front. Endocrinol.* **13**, 989626 (2022).
16. Krzeptowski, W. et al. Proximity ligation assay detection of protein–DNA interactions—is there a link between heme oxygenase-1 and G-quadruplexes? *Antioxidants* **10**, 94 (2021).
17. Ooki, T. & Hatakeyama, M. Protocol for visualizing conditional interaction between transmembrane and cytoplasmic proteins. *STAR Protoc.* **2**, 100430 (2021).
18. Vistain, L. et al. Quantification of extracellular proteins, protein complexes and mRNAs in single cells by proximity sequencing. *Nat. Methods* **19**, 1578–1589 (2022).
19. Söderberg, O. et al. Direct observation of individual endogenous protein complexes in situ by proximity ligation. *Nat. Methods* **3**, 995–1000 (2006).
20. Fredriksson, S. Visualizing signal transduction pathways by quantifying protein–protein interactions in native cells and tissue. *Nat. Methods* **6**, i–ii (2009).
21. Alam, M. S. Proximity Ligation Assay (PLA). *Curr. Protoc. Immunol.* **123**, e58 (2018).
22. Cai, S. et al. Multiplexed protein profiling reveals spatial subcellular signaling networks. *iScience* **25**, 104980 (2022).
23. Baker, S. J., Poulikakos, P. I., Irie, H. Y., Parekh, S. & Reddy, E. P. CDK4: a master regulator of the cell cycle and its role in cancer. *Genes Cancer* **13**, 21–45 (2022).
24. Brown, K. et al. Population pharmacokinetics and exposure-response of osimertinib in patients with non-small cell lung cancer. *Br. J. Clin. Pharm.* **83**, 1216–1226 (2017).
25. Shi, P. et al. Overcoming acquired resistance to AZD9291, a third generation EGFR inhibitor, through modulation of MEK/ERK-dependent Bim and Mcl-1 degradation. *Clin. Cancer Res.* **23**, 6567–6579 (2017).
26. Willis, S. N. et al. Proapoptotic Bak is sequestered by Mcl-1 and Bcl-xL, but not Bcl-2, until displaced by BH3-only proteins. *Genes Dev.* **19**, 1294–1305 (2005).
27. Hwang, H. C. & Clurman, B. E. Cyclin E in normal and neoplastic cell cycles. *Oncogene* **24**, 2776–2786 (2005).
28. Zhu, L. et al. Targeting c-Myc to overcome acquired resistance of EGFR mutant NSCLC cells to the third generation EGFR tyrosine kinase inhibitor, osimertinib. *Cancer Res.* **81**, 4822–4834 (2021).
29. Li, J.-Q., Miki, H., Ohmori, M., Wu, F. & Funamoto, Y. Expression of cyclin E and cyclin-dependent kinase 2 correlates with metastasis and prognosis in colorectal carcinoma. *Hum. Pathol.* **32**, 945–953 (2001).
30. Xie, X., Shu, R., Yu, C., Fu, Z. & Li, Z. Mammalian AKT, the emerging roles on mitochondrial function in diseases. *Aging Dis.* **13**, 157–174 (2022).
31. Yuan, Q., Chen, J., Zhao, H., Zhou, Y. & Yang, Y. Structure-aware protein–protein interaction site prediction using deep graph convolutional network. *Bioinformatics* **38**, 125–132 (2021).
32. Huang, Y., Wuchty, S., Zhou, Y. & Zhang, Z. SGPPI: structure-aware prediction of protein–protein interactions in rigorous conditions with graph convolutional network. *Brief. Bioinform.* **24**, bbad020 (2023).
33. Wang, R.-H., Luo, T., Zhang, H.-L. & Du, P.-F. PLA-GNN: computational inference of protein subcellular location alterations under drug treatments with deep graph neural networks. *Comput. Biol. Med.* **157**, 106775 (2023).
34. Fang, Z. et al. Subcellular spatially resolved gene neighborhood networks in single cells. *Cell Rep. Methods* **3**, 100476 (2023).
35. Burkhart, J. G. et al. Biology-inspired graph neural network encodes reactome and reveals biochemical reactions of disease. *Patterns* **4**, 100758 (2023).
36. Black, S. et al. CODEX multiplexed tissue imaging with DNA-conjugated antibodies. *Nat. Protoc.* **16**, 3802–3835 (2021).
37. Topacio, B. R. et al. Cyclin D-Cdk4,6 drives cell-cycle progression via the retinoblastoma protein's C-terminal helix. *Mol. Cell* **74**, 758–770.e4 (2019).
38. Christian, F., Smith, E. L. & Carmody, R. J. The regulation of NF-κB subunits by phosphorylation. *Cells* **5**, 12 (2016).
39. Zhang, S., Xiong, X. & Sun, Y. Functional characterization of SOX2 as an anticancer target. *Sig. Transduct. Target. Ther.* **5**, 135 (2020).
40. Li, L. et al. Protective autophagy decreases osimertinib cytotoxicity through regulation of stem cell-like properties in lung cancer. *Cancer Lett.* **452**, 191–202 (2019).
41. Frank, D. O. et al. The pro-apoptotic BH3-only protein Bim interacts with components of the Translocase of the Outer Mitochondrial Membrane (TOM). *PLoS ONE* **10**, e0123341 (2015).
42. Lalier, L. et al. TOM20-mediated transfer of Bcl2 from ER to MAM and mitochondria upon induction of apoptosis. *Cell Death Dis.* **12**, 182 (2021).
43. Smith, M. A. et al. Annotation of human cancers with EGFR signaling-associated protein complexes using proximity ligation assays. *Sci. Signal.* **8**, ra4 (2015).
44. Yuan, X. et al. Developing TRAIL/TRAIL-death receptor-based cancer therapies. *Cancer Metastasis Rev.* **37**, 733–748 (2018).
45. Zhang, X., Tang, N., Hadden, T. J. & Rishi, A. K. Akt, FoxO and regulation of apoptosis. *Biochim. Biophys. Acta* **1813**, 1978–1986 (2011).
46. Jacobsen, K. et al. Convergent Akt activation drives acquired EGFR inhibitor resistance in lung cancer. *Nat. Commun.* **8**, 410 (2017).
47. Xu, R. et al. SIRT1/PGC-1α/PPAR-γ correlate with hypoxia-induced chemoresistance in non-small cell lung cancer. *Front. Oncol.* **11**, 682762 (2021).
48. Lu, A. & Pfeffer, S. R. Golgi-associated RhoBTB3 targets Cyclin E for ubiquitylation and promotes cell cycle progression. *J. Cell Biol.* **203**, 233–250 (2013).

49. Makhoul, C. & Gleeson, P. A. Regulation of mTORC1 activity by the Golgi apparatus. *Fac. Rev.* **10**, 50 (2021).
50. Hagey, D. W. & Muhr, J. Sox2 acts in a dose-dependent fashion to regulate proliferation of cortical progenitors. *Cell Rep.* **9**, 1908–1920 (2014).
51. Chen, C., Weiss, S. T. & Liu, Y.-Y. Graph convolutional network-based feature selection for high-dimensional and low-sample size data. *Bioinformatics* **39**, btad135 (2023).
52. Blakely, D., Lanchantin, J. & Qi, Y. Time and space complexity of graph convolutional networks. *GitHub* https://qdata.github.io/deep2Read/talks-mb2019/Derrick_201906_GCN_complexityAnalysis-writeup.pdf (2019).
53. Xiao, X., Wu, Y., Shen, F., MuLaTiAize, Y. & Xinhua, N. Osimertinib improves the immune microenvironment of lung cancer by downregulating PD-L1 expression of vascular endothelial cells and enhances the antitumor effect of bevacizumab. *J. Oncol.* **2022**, 1531353 (2022).
54. Hsu, P.-C. et al. YAP promotes erlotinib resistance in human non-small cell lung cancer cells. *Oncotarget* **7**, 51922–51933 (2016).
55. Wang, C. et al. Verteporfin inhibits YAP function through up-regulating 14-3-3σ sequestering YAP in the cytoplasm. *Am. J. Cancer Res.* **6**, 27–37 (2015).
56. Huang, Y., Ahmad, U. S., Rehman, A., Uttagomol, J. & Wan, H. YAP inhibition by verteporfin causes downregulation of desmosomal genes and proteins leading to the disintegration of intercellular junctions. *Life* **12**, 792 (2022).
57. Önel, T., Yıldırım, E. & Yaba, A. P-049 Verteporfin suppresses cell proliferation, survival and migration of TCam-2 human seminoma cells via inhibits the YAP-TEAD complex. *Hum. Reprod.* **38**, dead093.414 (2023).
58. Kim, J. et al. Hot spot analysis of YAP-TEAD protein–protein interaction using the fragment molecular orbital method and its application for inhibitor discovery. *Cancers* **13**, 4246 (2021).
59. Zhang, H. et al. Tumor-selective proteotoxicity of verteporfin inhibits colon cancer progression independently of YAP1. *Sci. Signal.* **8**, ra98 (2015).
60. Tian, X. et al. E-cadherin/β-catenin complex and the epithelial barrier. *J. Biomed. Biotechnol.* **2011**, 567305 (2011).
61. Azimi, I., Roberts-Thomson, S. J. & Monteith, G. R. Calcium influx pathways in breast cancer: opportunities for pharmacological intervention. *Br. J. Pharmacol.* **171**, 945–960 (2014).
62. Zhao, M., Finlay, D., Zharkikh, I. & Vuori, K. Novel role of Src in priming Pyk2 phosphorylation. *PLoS ONE* **11**, e0149231 (2016).
63. Momin, A. A. et al. PYK2 senses calcium through a disordered dimerization and calmodulin-binding element. *Commun. Biol.* **5**, 800 (2022).
64. Lee, D. & Hong, J.-H. Activated PyK2 and its associated molecules transduce cellular signaling from the cancerous milieu for cancer metastasis. *Int. J. Mol. Sci.* **23**, 15475 (2022).
65. Hu, X., Li, J., Fu, M., Zhao, X. & Wang, W. The JAK/STAT signaling pathway: from bench to clinic. *Sig. Transduct. Target. Ther.* **6**, 402 (2021).
66. Mengie Ayele, T., Tilahun Muche, Z., Behaile Teklemariam, A., Bogale Kassie, A. & Chekol Abebe, E. Role of JAK2/STAT3 signaling pathway in the tumorigenesis, chemotherapy resistance, and treatment of solid tumors: a systemic review. *J. Inflamm. Res.* **15**, 1349–1364 (2022).
67. Whitaker, R. H. & Cook, J. G. Stress relief techniques: p38 MAPK determines the balance of cell cycle and apoptosis pathways. *Biomolecules* **11**, 1444 (2021).
68. Zhou, X. et al. Highly sensitive spatial transcriptomics using FISHnCHIPs of multiple co-expressed genes. *Nat. Commun.* **15**, 2342 (2024).
69. Hu, T. et al. Single-cell spatial metabolomics with cell-type specific protein profiling for tissue systems biology. *Nat. Commun.* **14**, 8260 (2023).
70. Lischetti, U. et al. Dynamic thresholding and tissue dissociation optimization for CITE-seq identifies differential surface protein abundance in metastatic melanoma. *Commun. Biol.* **6**, 830 (2023).
71. Park, P. J. ChIP–seq: advantages and challenges of a maturing technology. *Nat. Rev. Genet.* **10**, 669–680 (2009).
72. Wang, P., Yang, Y., Hong, T. & Zhu, G. Proximity ligation assay: an ultrasensitive method for protein quantification and its applications in pathogen detection. *Appl. Microbiol. Biotechnol.* **105**, 923–935 (2021).
73. Karlsson, F. et al. Molecular pixelation: spatial proteomics of single cells by sequencing. *Nat. Methods* **21**, 1044–1052 (2024).
74. Mo, X. et al. Systematic discovery of mutation-directed neo-protein-protein interactions in cancer. *Cell* **185**, 1974–1985. e12 (2022).
75. Lee, H.-W. et al. Real-time single-molecule co-immunoprecipitation analyses reveal cancer-specific Ras signalling dynamics. *Nat. Commun.* **4**, 1505 (2013).
76. Free, R. B., Hazelwood, L. A. & Sibley, D. R. Identifying novel protein–protein interactions using co-immunoprecipitation and mass spectroscopy. *Curr. Protoc. Neurosci.* https://doi.org/10.1002/0471142301.ns0528s46 (2009).
77. Johnson, K. L. et al. Revealing protein–protein interactions at the transcriptome scale by sequencing. *Mol. Cell* **81**, 4091–4103.e9 (2021).
78. Zhang, B., Park, B.-H., Karpinets, T. & Samatova, N. F. From pull-down data to protein interaction networks and complexes with biological relevance. *Bioinformatics* **24**, 979–986 (2008).
79. Jain, A., Liu, R., Xiang, Y. K. & Ha, T. Single-molecule pull-down for studying protein interactions. *Nat. Protoc.* **7**, 445–452 (2012).
80. Yachie, N. et al. Pooled-matrix protein interaction screens using Barcode Fusion Genetics. *Mol. Syst. Biol.* **12**, 863 (2016).
81. Lievens, S. et al. Array MAPPIT: high-throughput interactome analysis in mammalian cells. *J. Proteome Res.* **8**, 877–886 (2009).
82. Wu, Y., Li, Q. & Chen, X.-Z. Detecting protein–protein interactions by far western blotting. *Nat. Protoc.* **2**, 3278–3284 (2007).
83. Kristensen, A. R., Gsponer, J. & Foster, L. J. A high-throughput approach for measuring temporal changes in the interactome. *Nat. Methods* **9**, 907–909 (2012).
84. Miura, K. An overview of current methods to confirm protein–protein interactions. *Protein Pept. Lett.* **25**, 728–733 (2018).
85. Qin, W., Myers, S. A., Carey, D. K., Carr, S. A. & Ting, A. Y. Spatiotemporally-resolved mapping of RNA binding proteins via functional proximity labeling reveals a mitochondrial mRNA anchor promoting stress recovery. *Nat. Commun.* **12**, 4980 (2021).
86. Kaewsapsak, P., Shechner, D. M., Mallard, W., Rinn, J. L. & Ting, A. Y. Live-cell mapping of organelle-associated RNAs via proximity biotinylation combined with protein-RNA crosslinking. *eLife* **6**, e29224 (2017).
87. Roux, K. J., Kim, D. I., Burke, B. & May, D. G. BioID: a screen for protein–protein interactions. *Curr. Protoc. Protein Sci.* **91**, 19.23.1–19.23.15 (2018).
88. Cho, K. F. et al. Proximity labeling in mammalian cells with TurboID and split-TurboID. *Nat. Protoc.* **15**, 3971–3999 (2020).
89. Park, S.-H., Ko, W., Lee, H. S. & Shin, I. Analysis of protein–protein interaction in a single live cell by using a FRET system based on genetic code expansion technology. *J. Am. Chem. Soc.* **141**, 4273–4281 (2019).
90. Mo, X.-L. & Fu, H. in *High Throughput Screening: Methods and Protocols* (ed. Janzen, W. P.) 263–271 (Springer, 2016).
91. ul Ain Farooq, Q., Shaukat, Z., Aiman, S. & Li, C.-H. Protein–protein interactions: methods, databases, and applications in virus-host study. *World J. Virol.* **10**, 288–300 (2021).

92. Muhlich, J. L. et al. Stitching and registering highly multiplexed whole-slide images of tissues and tumors using ASHLAR. *Bioinformatics* **38**, 4613–4621 (2022).
93. Stringer, C., Wang, T., Michaelos, M. & Pachitariu, M. Cellpose: a generalist algorithm for cellular segmentation. *Nat. Methods* **18**, 100–106 (2021).
94. Greenwald, N. F. et al. Whole-cell segmentation of tissue images with human-level performance using large-scale data annotation and deep learning. *Nat. Biotechnol.* **40**, 555–565 (2022).
95. Bannon, D. et al. DeepCell Kiosk: scaling deep learning-enabled cellular image analysis with Kubernetes. *Nat. Methods* **18**, 43–45 (2021).
96. Graham, S. et al. Hover-Net: simultaneous segmentation and classification of nuclei in multi-tissue histology images. *Med. Image Anal.* **58**, 101563 (2019).
97. Kipf, T. N. & Welling, M. Semi-supervised classification with graph convolutional networks. Preprint at https://arxiv.org/abs/1609.02907 (2017).
98. Veličković, P. et al. Graph attention networks. Preprint at https://arxiv.org/abs/1710.10903 (2018).
99. Xu, K., Hu, W., Leskovec, J. & Jegelka, S. How powerful are graph neural networks? Preprint at https://arxiv.org/abs/1810.00826 (2019).
100. Morris, C. et al. Weisfeiler and Leman go neural: higher-order graph neural networks. In *Proceedings of the AAAI Conference on Artificial Intelligence* 4602–4609 (2019).
101. Hamilton, W. L., Ying, R. & Leskovec, J. Inductive representation learning on large graphs. In *Proceedings of the 31st International Conference on Neural Information Processing Systems* 1025–1035 (2017).
102. Li, Y., Tarlow, D., Brockschmidt, M. & Zemel, R. Gated graph sequence neural networks. Preprint at https://arxiv.org/abs/1511.05493v4 (2017).
103. Hu, G. et al. Attribute-enhanced face recognition with neural tensor fusion networks. In *2017 IEEE International Conference on Computer Vision (ICCV)* 3764–3773 (IEEE, 2017).
104. Chen, R. J. et al. Pathomic Fusion: an integrated framework for fusing histopathology and genomic features for cancer diagnosis and prognosis. *IEEE Trans. Med. Imaging* **41**, 757–770 (2022).
105. Cai, S. et al. iseqPLA. *figshare* https://figshare.com/s/d58cb4376bb235c74ee6 (2024).
106. Cai, S. et al. iseqPLA. *GitHub* https://github.com/coskunlab/iseqPLA (2024).

Acknowledgements

A.F.C. acknowledges a Career Award from the Scientific Interface of Burroughs Wellcome Fund and a Bernie-Marcus Early-Career Professorship. A.F.C. was supported by start-up funds from the Georgia Institute of Technology and Emory University. Research reported in this publication was supported by Lung Spore and the National Cancer Institute of the National Institutes of Health under Award Number P50CA217691 from the Career Enhancement Program, R33CA291197, NSF CAREER and R35GM151028. The content is solely the responsibility of the authors and does not necessarily represent the official views of the National Institutes of Health. Research reported in this publication was supported in part by the Cancer Tissue and Pathology Shared Resource and the Data and Technology Applications Shared Resource of Winship Cancer Institute of Emory University and NIH/NCI under award number P30CA138292.

Author contributions

S.C., T.H., F.G.R.M., E.O. and A.F.C. designed experiments, analysed data and wrote the manuscript. M.W. analysed data. Y.-T.O. designed experiments and analysed data. S.C., A.V., F.G.R.M., N.Z., T.Z., S.D., A.P. and Y.-T.O. conducted experiments. S.C., T.H., A.F.C., F.S., S.S.R. and S.-Y.S. contributed materials.

Competing interests

A.F.C., S.C. and T.H. declare a patent application related to the spatial-signalling interactomics assay (US Provisional 63/399,427 and US Application No. 18/452,178). The other authors declare no competing interests.

Additional information

Extended data is available for this paper at https://doi.org/10.1038/s41551-024-01271-x.

Supplementary information The online version contains supplementary material available at https://doi.org/10.1038/s41551-024-01271-x.

Correspondence and requests for materials should be addressed to Ahmet F. Coskun.

Peer review information *Nature Biomedical Engineering* thanks Feixiong Cheng, Xiangxiang Zeng and the other, anonymous, reviewer(s) for their contribution to the peer review of this work. Peer reviewer reports are available.

https://doi.org/10.1038/s41551-024-01271-x

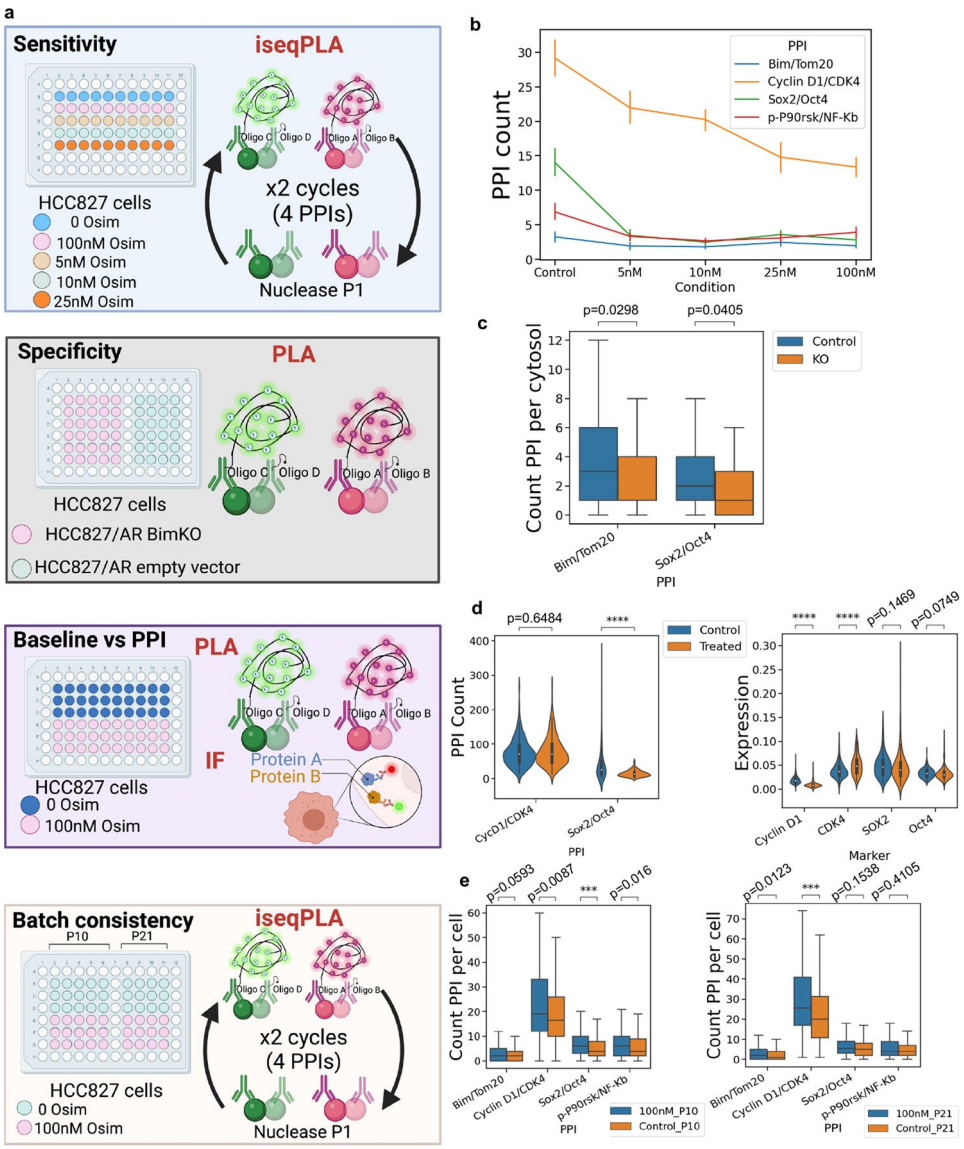

Extended Data Fig. 1 | Evaluation of iseqPLA properties in HCC827 cells. a, Visualization of the workflow evaluating PLA sensitivity, specificity, baseline vs PPI, and batch consistency in HCC827 cells. Following different treatments, the cells were stained with PLA or IF. The detailed experimental designs are in Supplementary Fig. 6a, 7a, 8a, and 9a, Created with BioRender.com. **b**, The comparison of PPI counts in HCC827 cells between those treated with a range of Osimertinib for 12 hours. The detailed results are in Supplementary Fig. 6. **c**, The comparison of PPI counts in two HCC827AR cells. The detailed results are in Supplementary Fig. 7. **d**, The comparison of PPI counts in HCC827 cells between those treated with and without Osimertinib. The baseline levels of 4 proteins in HCC827 cells with and without treatment were quantified on the right panel. The detailed results are in Supplementary Fig. 8. **e**, The comparison of PPI counts from 4 pairs in HCC827 cells from two batches treated with and without 12-hour Osimertinib. The detailed results are in Supplementary Fig. 9. Statistical testing was performed using Mann Whitney Wilcoxon Test two-sided (***: 0.0001 < p <= 0.001, ****: p < =0.0001). Box plots and violin plots: median (horizontal line inside box), 25th and 75th percentiles (box), 25th and 75th percentiles ±1.5 times the interquartile range (whiskers).

https://doi.org/10.1038/s41551-024-01271-x

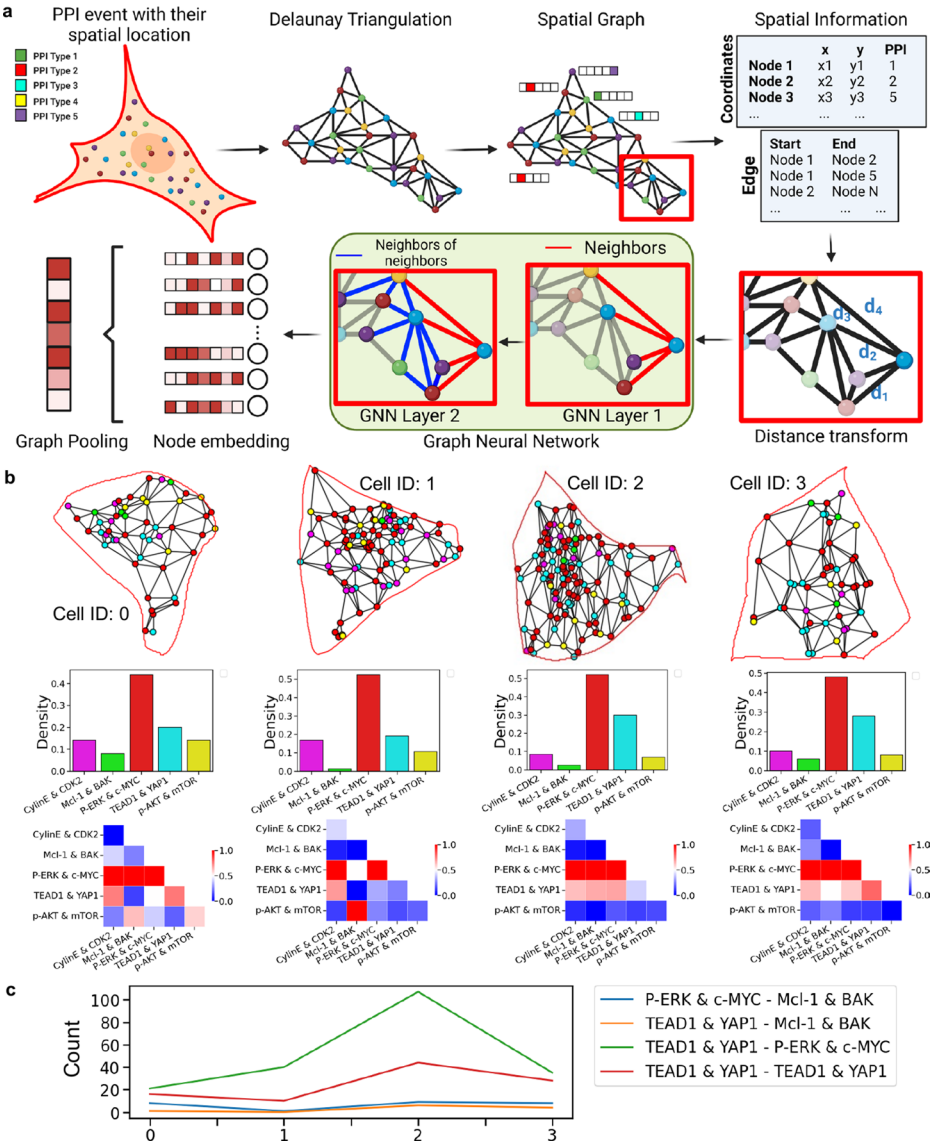

Extended Data Fig. 2 | Schematics showing the graphical implementation of spatial neighbouring information. a, Schematic showing the PPI events spatial information incorporated in the graph representation of PPI spatial neighbourhood. During each step of the spPPI-GNN, from the spatial graph, each PPI neighbour's embedding is incorporated until a global cell-level embedding is extracted and used for prediction. Created with BioRender.com. **b**, Example of cell PPI events spatial graph showing similar PPI event type density with different PPI event neighbours' distribution. This shows a spatial distribution heterogeneity of PPI events at the subcellular level. **c**, Line plot showing the variation of PPI type neighbouring count across cells (x-axis: cell ID) showed in **b**.

https://doi.org/10.1038/s41551-024-01271-x

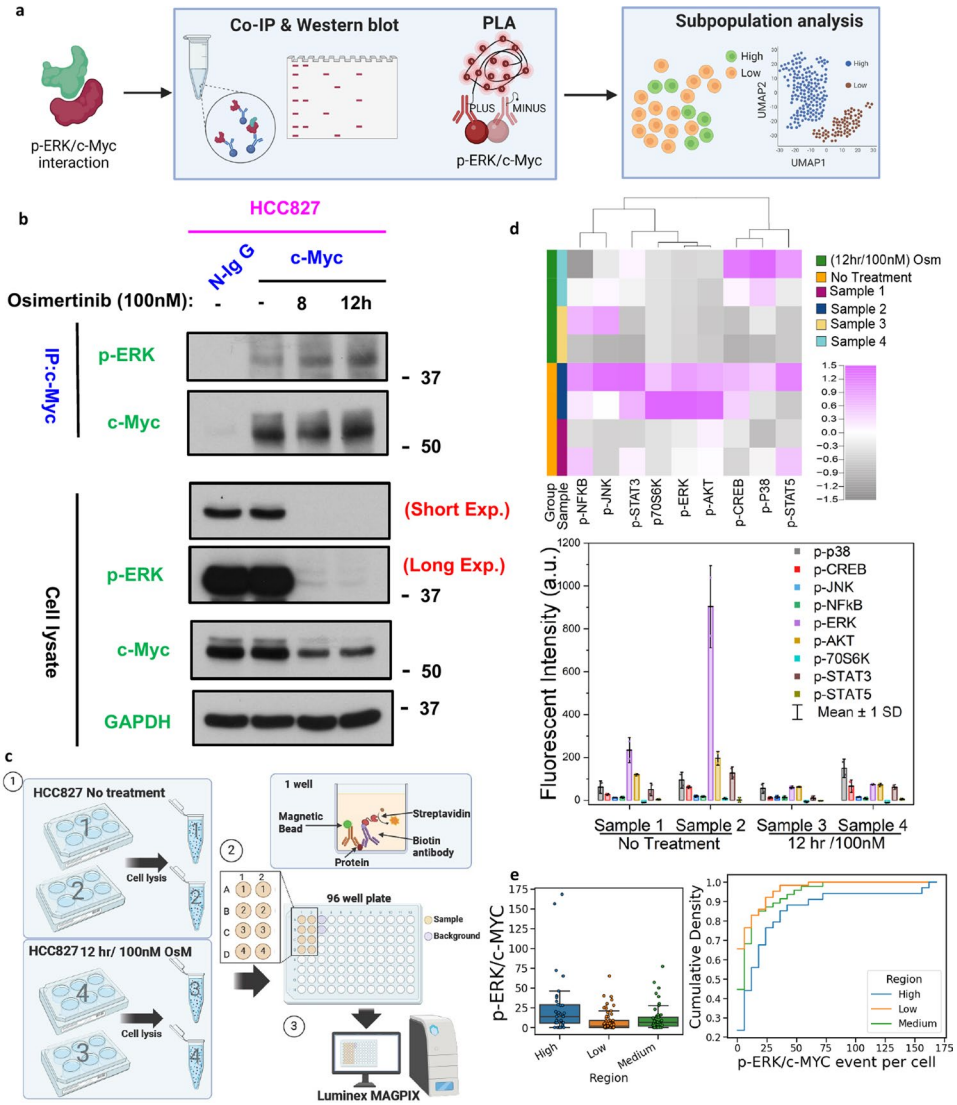

Extended Data Fig. 3 | Orthogonal validation of p-ERK/c-Myc interaction and expression in HCC827 cells. a, Schematic illustration of measuring p-ERK/c-Myc interaction using co-IP and PLA, Created with BioRender.com. **b**, Top Panel of western blots depicted results of co-IP of p-ERK and c-Myc in c-Myc pull-down samples. The cells were treated with 100 nM Osimertinib for 0, 8 12 hours. N-IgG served as a negative control for co-IP. The bottom panel demonstrated the results of p-ERK, c-Myc, and GAPDH expression run on different gels from the same HCC827 cell lysate. GAPDH was used as a negative control. P-ERK expressions at short and long exposure were shown in the gel. **c**, Workflow of measuring 9 phosphorylated proteins in HCC827 cells using Luminex. Created with BioRender.com. **d**, Quantification of 9 phosphorylated proteins in HCC827 cells treated with and without 12-hour 100 nM Osimertinib was shown in the heatmap and bar graph. Bar graphs are shown as mean ±1 SD. **e**, Quantification of p-ERK/c-Myc PPI counts in different ROIs with a high, low, and medium expression of p-ERK/c-Myc in HCC827 cells. The right graph shows the cumulative density which measures the percentage of cells expressing different numbers of p-ERK/c-Myc events per cell across three ROIs. The detailed statistics for each ROI are shown in Supplementary Fig. 25. Box plots: median (horizontal line inside box), 25th and 75th percentiles (box), 25th and 75th percentiles ±1.5 times the interquartile range (whiskers).

https://doi.org/10.1038/s41551-024-01271-x

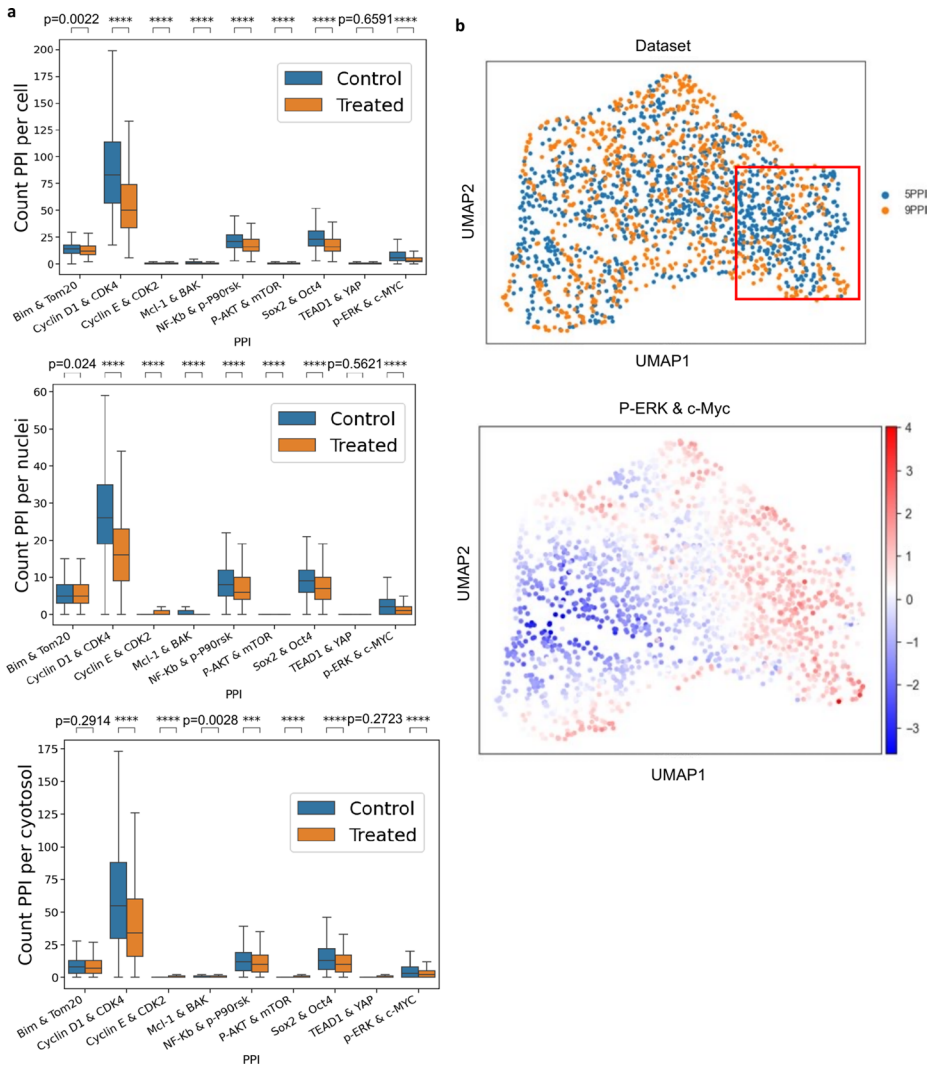

Extended Data Fig. 4 | Quantification of 26-plex profiling for 9 PPIs and 8 signalling and organelle markers in HCC827. a, The comparison of PPI counts in HCC827 whole cells, nuclei, and cytosol between those treated with and without Osimertinib. Statistical testing was performed using Mann Whitney Wilcoxon Test two-sided (***: 0.0001 < p <= 0.001, ****: p < =0.0001). The total cell numbers are 836 and 655 for untreated and Osimertinib-treated cells in the comparison of PPI count per cell. **b**, UMAP visualizes the similarity of p-ERK/c-Myc counts in the 5PPI and 9PPI datasets. Box plots: median (horizontal line inside box), 25th and 75th percentiles (box), 25th and 75th percentiles ±1.5 times the interquartile range (whiskers).

https://doi.org/10.1038/s41551-024-01271-x

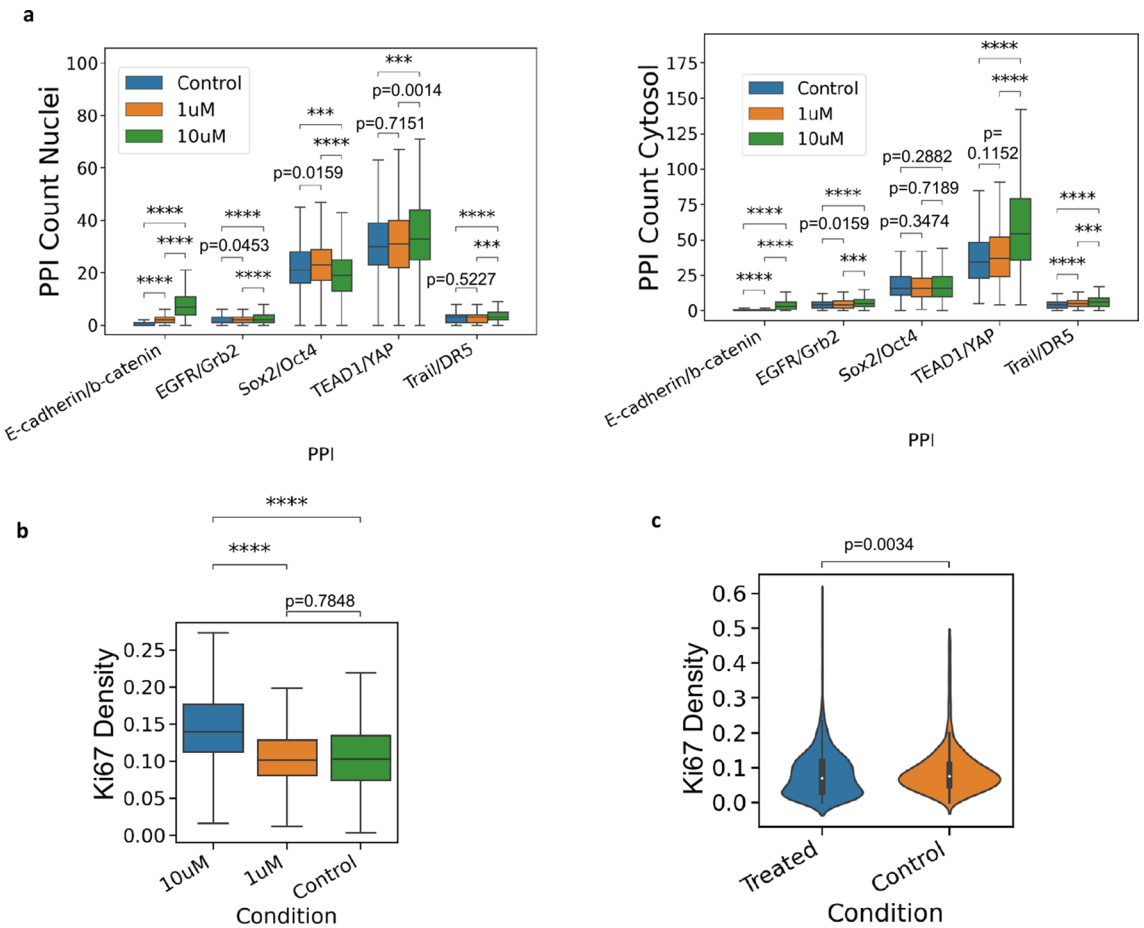

Extended Data Fig. 5 | Quantification of PPIs and Ki67 in HCC827 cells. a, The PPI count comparison in cytosol and nuclei is separately shown in the figure. The HCC827 cells were treated with VP at 0, 1, and 10 μM for 24 hours. **b**, The comparison of Ki67 density in HCC827 cells treated with and without VP. Ki67 density was calculated by dividing the Ki67 positive regions by the nuclear size. **c**, The comparison of Ki67 density in HCC827 cells treated with and without 100 nM Osimertinib for 12 hours. Statistical testing was performed using Mann Whitney Wilcoxon Test two-sided (***: 0.0001 < p <= 0.001, ****: p < =0.0001). Box plots and violin plots: median (horizontal line inside box), 25th and 75th percentiles (box), 25th and 75th percentiles ±1.5 times the interquartile range (whiskers).

https://doi.org/10.1038/s41551-024-01271-x

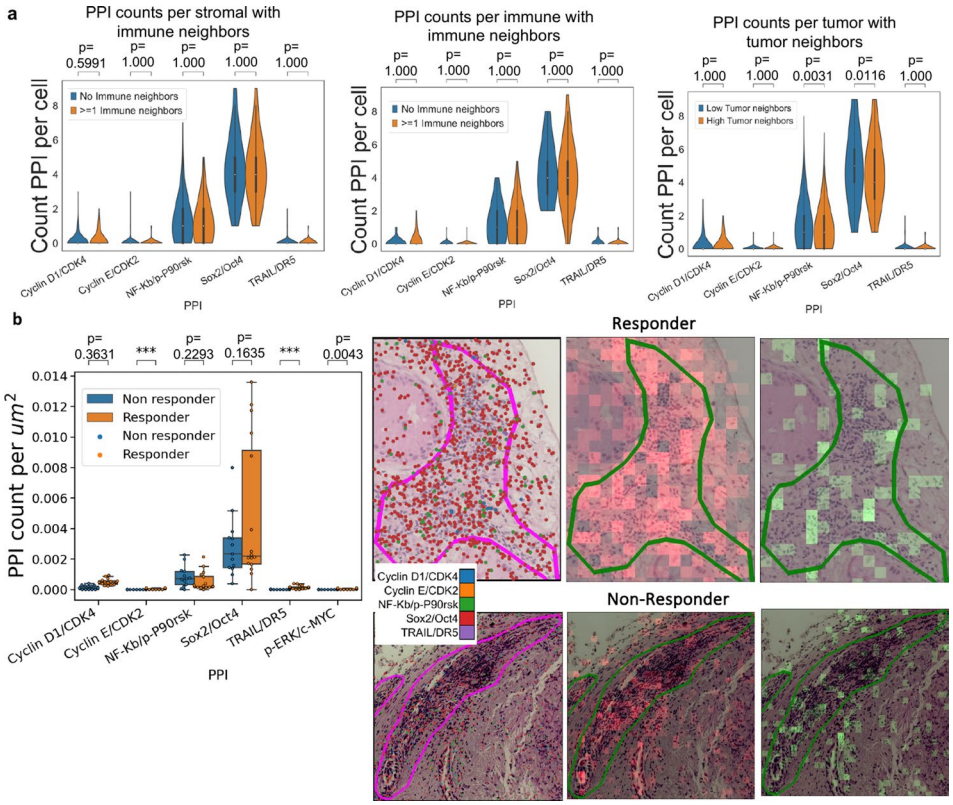

Extended Data Fig. 6 | PPI counts per cell and PPI density in patient tissues. **a**, Quantification of PPI counts per stromal, per immune cell with immune neighbours, and PPI counts per tumour cell with tumour neighbours at the single cell level in the responder tissue. Statistical testing was performed using t-test independent samples with Bonferroni correction (***: 0.0001 < p <= 0.001, ****: p < =0.0001). **b**, Comparison of the density of PPI counts in lymphocyte-enriched regions between responders and non-responders. A plot with a wider y-axis range is in Supplementary Fig. 40d to show the complete individual data points. Example images of 5 PPIs expression in lymphocyte-enriched regions are shown on the right. The first column is the visualization of 5 PPIs in lymphocyte-enriched regions. The second column displays the distributions of Sox2/Oct4 PPI in red. The third column exhibits the distributions of NF-kB/p-P90RSK PPIs in green. Statistical testing was performed using t-test independent samples (***: 0.0001 < p <= 0.001, ****: p < =0.0001). Box plots and Violin plots: median (horizontal line inside box), 25th and 75th percentiles (box), 25th and 75th percentiles ±1.5 times the interquartile range (whiskers).

nature portfolio

Corresponding author(s): Ahmet Coskun

Last updated by author(s): Aug 23, 2024

Reporting Summary

Nature Portfolio wishes to improve the reproducibility of the work that we publish. This form provides structure for consistency and transparency in reporting. For further information on Nature Portfolio policies, see our Editorial Policies and the Editorial Policy Checklist.

Statistics

For all statistical analyses, confirm that the following items are present in the figure legend, table legend, main text, or Methods section.

n/a	Confirmed	
☐	☒	The exact sample size (*n*) for each experimental group/condition, given as a discrete number and unit of measurement
☐	☒	A statement on whether measurements were taken from distinct samples or whether the same sample was measured repeatedly
☐	☒	The statistical test(s) used AND whether they are one- or two-sided *Only common tests should be described solely by name; describe more complex techniques in the Methods section.*
☐	☒	A description of all covariates tested
☐	☒	A description of any assumptions or corrections, such as tests of normality and adjustment for multiple comparisons
☐	☒	A full description of the statistical parameters including central tendency (e.g. means) or other basic estimates (e.g. regression coefficient) AND variation (e.g. standard deviation) or associated estimates of uncertainty (e.g. confidence intervals)
☐	☒	For null hypothesis testing, the test statistic (e.g. *F*, *t*, *r*) with confidence intervals, effect sizes, degrees of freedom and *P* value noted *Give P values as exact values whenever suitable.*
☒	☐	For Bayesian analysis, information on the choice of priors and Markov chain Monte Carlo settings
☐	☒	For hierarchical and complex designs, identification of the appropriate level for tests and full reporting of outcomes
☐	☒	Estimates of effect sizes (e.g. Cohen's *d*, Pearson's *r*), indicating how they were calculated

Our web collection on statistics for biologists contains articles on many of the points above.

Software and code

Policy information about availability of computer code

Data collection	Keyence Microscope BZ-X810 software was used for data collection. Python was used for data analysis.
Data analysis	The custom codes used in the study are available at https://github.com/coskunlab/iseqPLA.

For manuscripts utilizing custom algorithms or software that are central to the research but not yet described in published literature, software must be made available to editors and reviewers. We strongly encourage code deposition in a community repository (e.g. GitHub). See the Nature Portfolio guidelines for submitting code & software for further information.

Data

Policy information about availability of data

All manuscripts must include a data availability statement. This statement should provide the following information, where applicable:

- Accession codes, unique identifiers, or web links for publicly available datasets
- A description of any restrictions on data availability
- For clinical datasets or third party data, please ensure that the statement adheres to our policy

The main data supporting the results of this study are available within the paper and its Supplementary Information. The statistics needed to recreate the figures are provided as Source Data. The raw data are available from figshare at https://figshare.com/s/d58cb4376bb235c74ee6.

Research involving human participants, their data, or biological material

Policy information about studies with human participants or human data. See also policy information about sex, gender (identity/presentation), and sexual orientation and race, ethnicity and racism.

Reporting on sex and gender	The human specimens were obtained from male patients. Sex was not considered in the study design.
Reporting on race, ethnicity, or other socially relevant groupings	The human specimens were from White non-Hispanic men. Race, ethnicity and other socially relevant groupings were not considered in the study design.
Population characteristics	–
Recruitment	–
Ethics oversight	The use of human specimens was approved by the Institutional Review Board of Emory University (IRB00098377).

Note that full information on the approval of the study protocol must also be provided in the manuscript.

Field-specific reporting

Please select the one below that is the best fit for your research. If you are not sure, read the appropriate sections before making your selection.

☒ Life sciences ☐ Behavioural & social sciences ☐ Ecological, evolutionary & environmental sciences

For a reference copy of the document with all sections, see nature.com/documents/nr-reporting-summary-flat.pdf

Life sciences study design

All studies must disclose on these points even when the disclosure is negative.

Sample size	Sample sizes were chosen on the basis of the availability of biological specimens and resources.
Data exclusions	No data were excluded.
Replication	5 common pairs across 3 datasets in HCC827 cells.
Randomization	The study was not randomized, because it focused on specific cell lines and tissue samples with unique characteristics.
Blinding	The study was not blinded, because of the nature of experimental procedures.

Reporting for specific materials, systems and methods

We require information from authors about some types of materials, experimental systems and methods used in many studies. Here, indicate whether each material, system or method listed is relevant to your study. If you are not sure if a list item applies to your research, read the appropriate section before selecting a response.

Materials & experimental systems

n/a	Involved in the study
☐	☒ Antibodies
☒	☐ Eukaryotic cell lines
☒	☐ Palaeontology and archaeology
☒	☐ Animals and other organisms
☒	☐ Clinical data
☒	☐ Dual use research of concern
☒	☐ Plants

Methods

n/a	Involved in the study
☒	☐ ChIP-seq
☒	☐ Flow cytometry
☒	☐ MRI-based neuroimaging

Antibodies

Antibodies used	The vendors and catalogue numbers of the antibodies used are listed in Methods.

Validation	The optimization of the antibody-staining conditions is described in Methods. Supplementary table 1 provides the dilution-rate optimization.